

Mantle rheology and the scaling of bending dissipation in plate tectonics

I. R. Rose^{1,2} and J. Korenaga¹

Received 17 September 2010; revised 2 March 2011; accepted 4 April 2011; published 22 June 2011.

[1] Plate tectonics on Earth involves the bending deformation of plates at subduction zones, and because plates are generally considered to be stiff owing to the rheology of mantle minerals, the role of energy dissipation by plate bending in the global energy balance has been frequently debated in the recent literature. Here we consider how bending dissipation should scale with slab parameters such as dip angle, plate age, the radius of curvature, and plate velocity by systematically exploring the parameter space with instantaneous Stokes flow calculations. We derive the scaling of bending dissipation for a range of mantle viscosity functions, including pseudoplastic rheology with olivine flow laws. Our results indicate that, as we move away from the isoviscous case, the scaling gradually deviates from what has commonly been assumed in previous studies, most notably for the radius exponent, which exhibits more than threefold reduction and even a sign reversal in some cases. These modifications in scaling exponents originate in the complication of the deformation field caused by viscosity variations within the bending plate. Approximating the lithospheric rheology by a single effective viscosity in the dynamical models of subduction has been a common practice, but we suggest that such approximation may limit the geological relevance of modeling studies, in particular when estimating the significance of bending dissipation.

Citation: Rose, I. R., and J. Korenaga (2011), Mantle rheology and the scaling of bending dissipation in plate tectonics, *J. Geophys. Res.*, 116, B06404, doi:10.1029/2010JB008004.

1. Introduction

[2] Plate tectonics is the surface expression of a peculiar mode of thermal convection that is taking place in Earth's mantle; the surface of Earth is broken into a dozen plates or so, and many of these plates are recycled back into the deep mantle at subduction zones whereas new plates are constantly accreted at mid-ocean ridges. The combined geological, geophysical, and geochemical evidence on the present-day operation of plate tectonics is overwhelming [e.g., Schubert *et al.*, 2001], but there remain significant questions to be answered, including when plate tectonics started in the Earth history [e.g., Condie and Pease, 2008], how it evolved in the past [e.g., Korenaga, 2006], and why it takes place on Earth to begin with [e.g., Bercovici, 2003]. What makes the operation of plate tectonics possible has long been puzzling because experimental constraints on the strength of mantle minerals generally suggest that surface plates may be too strong to bend and subduct [e.g., Kohlstedt *et al.*, 1995], and a number of studies have been conducted to understand the generation of plate tectonics using theory and observations [e.g., Bercovici *et al.*, 2000;

Tackley, 2000; Gurnis *et al.*, 2000; Solomatov, 2004; Korenaga, 2007; Landuyt *et al.*, 2008].

[3] One particularly debated topic is the energetics of subduction. The kinetic energy balance of thermal convection requires that the rate of potential energy release associated with hot upwelling and cold downwelling is balanced by the rate of viscous dissipation in the convecting system [Turcotte and Schubert, 1982; Solomatov, 1995], and the question here is how much of energy is dissipated by the bending of plate (or equivalently, oceanic lithosphere) at subduction zones. Some studies suggest that plate bending could consume a significant fraction of potential energy [e.g., Conrad and Hager, 1999; Becker *et al.*, 1999; Bellahsen *et al.*, 2005], thereby being the most important bottleneck for the operation of plate tectonics, whereas others suggest that bending dissipation is only of second order importance [e.g., Stegman *et al.*, 2006; Wu *et al.*, 2008; Capitanio *et al.*, 2009]. What is noteworthy in this ongoing debate is that the interpretation of modeling results in these studies, in which a variety of mantle rheology is assumed, is often based on the following scaling for bending dissipation [e.g., Conrad and Hager, 1999; Buffett, 2006]:

$$\Phi_{BD} \propto \left(\frac{h}{R}\right)^3 \eta v^2, \quad (1)$$

where h is plate thickness, R is the radius of curvature for bending, η is viscosity, and v is plate velocity. This is an approximate analytic expression for the bending dissipation

¹Department of Geology and Geophysics, Yale University, New Haven, Connecticut, USA.

²Now at Department of Earth and Planetary Science, University of California, Berkeley, California, USA.

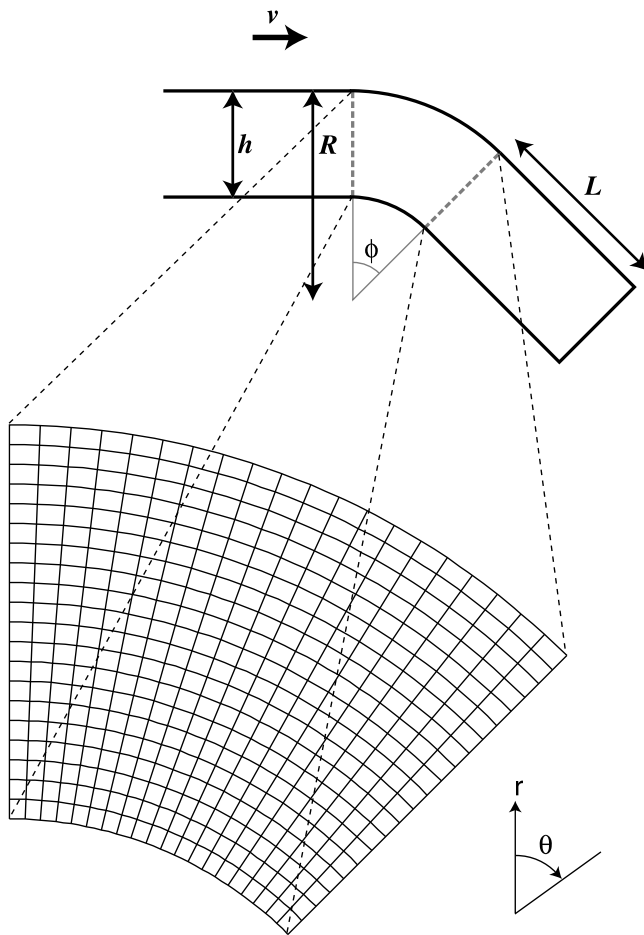


Figure 1. The geometry of an idealized subduction system considered in this study. A plate with thickness h moves with velocity v and bends with dip angle ϕ and the radius of curvature R . The length of the straight portion of the subducted plate is denoted by L . We calculate an instantaneous Stokes flow only for the bending part of the plate, the finite element discretization of which is illustrated schematically. In our polar coordinate system, the angular coordinate θ is measured clockwise from the north as shown.

of a plate with uniform viscosity, so its applicability is unclear when viscosity varies within a plate. The rheology of mantle minerals is a complex function of temperature, pressure, stress, grain size, and chemistry [e.g., Karato and Wu, 1993], and even though we may still be able to define an ‘effective’ viscosity for the bending part of a plate, whether the isoviscous scaling of (1) is valid with such effective viscosity is another issue.

[4] In this paper, we attempt to establish the scaling of bending dissipation as a function of mantle rheology, by a series of instantaneous Stokes flow calculations. Our results suggest that the scaling for realistic mantle rheology is likely to be very different from equation (1), and previous studies will be discussed in light of this new finding. The structure of this paper is the following. After describing our modeling strategy in section 2, we will present numerical results with increasingly complex viscosity functions and estimate corresponding scaling laws for bending dissipation. Global

bending dissipation in the present-day Earth will be discussed, as well as the meaning of effective lithospheric viscosity in plate tectonic convection. We will then revisit previous suggestions on the role of bending in plate tectonics.

2. Theoretical Formulation

2.1. Model Domain, Boundary Conditions, and Governing Equations

[5] To focus on energy dissipation in plate bending, an idealistic situation is assumed in which a plate of thickness h is moving at velocity v and subducting with a dip angle of ϕ (Figure 1). The radius of curvature for bending is denoted by R , and the length of a subducted plate by L . We consider only the deforming part of the plate (Figure 1) and solve for the internal deformation within the part by applying the free slip boundary condition to the top and bottom boundaries and the velocity of v uniformly along the side boundaries. We use free slip boundaries to exclude possible contributions from interplate friction at the top boundary and sublithospheric shearing at the bottom boundary; our intention is to focus on bending dissipation. Note that applying a constant angular velocity along the slab top does not produce plate bending. A necessary component of bending is compression of one side of the plate and extension of the other. Imposing a constant velocity on the slab top suppresses this extension-compression pairing, resulting in a purely angular flow field analogous to Couette flow in a cylinder. Instead, we impose constant incoming and outgoing velocity along the edges of the plates and require the radial velocity component to be zero along the slab top and bottom. These boundary conditions may be deemed more realistic, as the driving force of plate tectonics is the pulling force from the leading edge of the plate, rather than some traction on the top surface. Our boundary conditions are still kinematic, so unlike a fully dynamic model, a given plate velocity is not necessarily consistent with other slab parameters such as dip angle and plate thickness. This lack of internal consistency does not pose any problem, however, because our purpose is simply to measure bending dissipation as a function of given slab parameters. Scaling derived from this flow calculation can be used to analyze the results of fully dynamic models (section 4.3).

[6] Because the mantle has a very high Prandtl number, the inertial terms in the equation of motion are negligible, and the velocity field, \mathbf{u} , can be determined by solving the following Stokes flow equations consist of the conservation of mass,

$$\nabla \cdot \mathbf{u} = 0, \quad (2)$$

and the conservation of momentum,

$$-\nabla P + \nabla \cdot [\eta(\nabla \mathbf{u} + \nabla \mathbf{u}^T)] = 0, \quad (3)$$

where P is dynamic pressure and η is viscosity. All the differential operators are in a polar coordinate (r, θ) system, which is a natural choice given our model geometry. As we focus on deformation caused by the applied boundary conditions, we do not consider external force in the momentum balance.

[7] Assuming half-space cooling [e.g., *Turcotte and Schubert*, 1982], the thermal structure of the bending plate is given by

$$T(r) = T_s + \Delta T \operatorname{erf}\left(\frac{R-r}{2\sqrt{\kappa t}}\right), \quad (4)$$

where T_s is surface temperature, ΔT is the temperature contrast difference between the surface and the asthenosphere, κ is thermal diffusivity, and t is the age of a plate at the point of subduction. We define the base of the plate with the temperature of $T_s + 0.9\Delta T$, so the thickness of the subducting plate is related to its age as

$$h = 2 \operatorname{erf}^{-1}(0.9)\sqrt{\kappa t} \approx 2.33\sqrt{\kappa t}. \quad (5)$$

[8] The model is nondimensionalized by introducing the following characteristic scales (starred variables are dimensionless),

$$\begin{aligned} r &= Rr^*; & T &= T_s + \Delta TT^*; & \mathbf{u} &= \frac{\kappa}{R} \mathbf{u}^*; \\ \eta &= \eta_r \eta^*; & P &= \frac{\eta_r \kappa}{R^2} P^*, \end{aligned} \quad (6)$$

where η_r is reference viscosity. The governing equations then become

$$\nabla \cdot \mathbf{u}^* = 0, \quad (7)$$

and

$$-\nabla P^* + \nabla \cdot [\eta^*(\nabla \mathbf{u}^* + \nabla \mathbf{u}^{*T})] = 0, \quad (8)$$

with the following boundary conditions,

$$\begin{aligned} u_\theta^*|_{\theta=0} &= u_\theta^*|_{\theta=\phi} = v^*; \\ u_r^*|_{\theta=0} &= u_r^*|_{\theta=\phi} = 0; \\ \tau_{r\theta}^*|_{r^*=1} &= \tau_{r\theta}^*|_{r^*=r_{\min}^*} = 0; \\ u_r^*|_{r^*=1} &= u_r^*|_{r^*=r_{\min}^*} = 0, \end{aligned} \quad (9)$$

where $\tau_{r\theta}^*$ is the shear stress component and $r_{\min}^* = 1 - h/R$.

[9] Viscous dissipation in the bending plate (per unit length along a trench) is given by

$$\Phi_{\text{BD}}^* = \int_{r_{\min}^*}^1 \int_0^\phi 2\eta^* [(e_{rr}^*)^2 + (e_{\theta\theta}^*)^2 + 2(e_{r\theta}^*)^2] r^* dr^* d\theta, \quad (10)$$

where the dissipation is scaled by $\eta_r \kappa^2 / R^2$ and e_{ij}^* denotes the dimensionless strain rate tensor defined as

$$\begin{aligned} e_{rr}^* &= \frac{\partial u_r^*}{\partial r^*}, \\ e_{\theta\theta}^* &= \frac{1}{r^*} \frac{\partial u_\theta^*}{\partial \theta} + \frac{u_r^*}{r^*}, \\ 2e_{r\theta}^* &= r^* \frac{\partial}{\partial r^*} \left(\frac{u_\theta^*}{r^*} \right) + \frac{1}{r^*} \frac{\partial u_r^*}{\partial \theta}. \end{aligned}$$

2.2. Mantle Rheology

[10] We use several different kinds of mantle rheology, starting from constant viscosity and gradually proceeding to

more elaborate ones. With constant viscosity, $\eta^* = 1$ everywhere, and this isoviscous case serves as a reference for more complex ones.

[11] For purely temperature-dependent viscosity, we use the following linear exponential form:

$$\eta^*(T^*) = \exp[\theta(1 - T^*)], \quad (11)$$

for which reference viscosity is defined at $T^* = 1$. The degree of temperature dependency is controlled by the Frank-Kamenetskii parameter θ (not to be confused with the angular component of the polar coordinates), which can be related to the activation energy E as [e.g., *Solomatov and Moresi*, 2000]

$$\theta = \frac{E\Delta T}{R_g(T_s + \Delta T)^2}, \quad (12)$$

where R_g is the universal gas constant.

[12] For realistic activation energy of few hundreds kJ mol⁻¹, the coldest part of the plate would be very stiff due to this temperature-dependent viscosity, but it can also deform by brittle failure. Following *Moresi and Solomatov* [1998], we assume that this brittle behavior can be modeled by nonlinear effective viscosity that is adjusted to ensure the stresses remain bounded by the yield stress envelope. The yield stress criterion for brittle deformation may be expressed as

$$\tau_y = c_0 + \mu\rho_0gz, \quad (13)$$

where c_0 is the cohesive strength, μ is the friction coefficient, ρ_0 is reference density, g is gravitational acceleration, and z is depth from Earth's surface. Using the length scale R and the stress scale $\eta_r \kappa / R^2$, the criterion may be nondimensionalized as

$$\tau_y^* = \tau_0^* + \tau_1^* z^*, \quad (14)$$

where

$$\tau_0^* = \frac{c_0 R^2}{\kappa \eta_r}, \quad (15)$$

and

$$\tau_1^* = \frac{\mu\rho_0 g R^3}{\kappa \eta_r} = \gamma R a_R. \quad (16)$$

Here γ is defined as

$$\gamma = \frac{\mu}{\alpha \Delta T}, \quad (17)$$

where α is thermal expansivity, and

$$R a_R = \frac{\alpha \rho g \Delta T R^3}{\kappa \eta_r}, \quad (18)$$

which may be called as the radius Rayleigh number. The depth z^* is calculated as $1 - r^* \cos \theta$. We assume the cohesive strength to be negligibly small compared to the depth-dependent component [e.g., *Byerlee*, 1978] and set τ_0^* to $\tau_1^* \times 10^{-5}$ (τ_0^* is not set to zero to avoid numerical insta-

bility). The nonlinear effective viscosity for the plastic deformation is calculated as

$$\eta_y^* = \frac{\tau_y^*}{e_{II}^*}, \quad (19)$$

where e_{II}^* is the second invariant of the strain rate tensor. Finally, pseudoplastic rheology that incorporates both plastic and ductile deformation is defined as the harmonic mean of the above effective viscosity and temperature-dependent viscosity,

$$\eta^*(T^*, z^*) = \left(\frac{1}{\eta_y^*} + \frac{1}{\eta_T^*} \right)^{-1}. \quad (20)$$

For temperature-dependent viscosity, we use either the linear exponential form (equation (11)) or the following Arrhenius form,

$$\eta^*(T^*) = \exp\left(\frac{E^*}{T^* + T_{\text{off}}^*} - \frac{E^*}{1 + T_{\text{off}}^*} \right), \quad (21)$$

where T_{off}^* is the surface temperature normalized by the temperature contrast (i.e., $T_s/\Delta T$), and $E^* = E/(R\Delta T)$. Flow calculations with nonlinear viscosity have to be iterated to obtain a self-consistent pair of viscosity and stress fields, and we typically conduct up to 10–20 iterations so that the root-mean-square (RMS) difference of velocity fields from successive iterations converges down to less than 0.1%.

[13] We further elaborate pseudoplastic rheology by incorporating experimental constraints on the rheology of olivine aggregates, which is commonly thought to represent the rheology of the upper mantle [Karato and Wu, 1993]. Effective olivine viscosity is first evaluated through the following composite rheological model:

$$\eta_{\text{ol}} = \sigma_{II} / (e_f + e_s + e_p), \quad (22)$$

where σ_{II} denotes the second invariant of the stress tensor, and e_f , e_s , and e_p are strain rates for diffusion, dislocation, and Peierls creep mechanisms, respectively. The strain rate for diffusion creep is given by

$$e_f = A_f \sigma_{II} d^{-p} \exp\left[-\frac{E_f + pV_f}{R_g T_a} \right], \quad (23)$$

where A_f is a preexponential factor, d is grain size, p is the grain size exponent, p is pressure, T_a is absolute temperature, and E_f and V_f are the activation energy and volume for diffusion creep, respectively. Here pressure is assumed to be lithostatic (i.e., $\rho_0 g z$), and absolute temperature is calculated by considering the effect of adiabatic compression as $T_a = T + (dT/dz)_{SZ}$ with the adiabatic gradient of 0.5 K km⁻¹. Similarly, the strain rate for dislocation creep is given by

$$e_s = A_s \sigma_{II}^n \exp\left[-\frac{E_s + pV_s}{R_g T_a} \right], \quad (24)$$

where n is the stress exponent, and that for Peierls creep is by

$$e_p = A_p \exp\left[-\frac{E_p}{R_g T_a} \left(1 - \frac{\sigma_{II}}{\sigma_P} \right)^2 \right], \quad (25)$$

where σ_P is the Peierls stress. This formula is valid only when $\sigma_{II} > 200$ MPa, and for stresses below this threshold, e_p is set to zero. For the Peierls creep, we use the following values: $A_p = 4.93 \times 10^{11} \text{ s}^{-1}$, $E_p = 536 \text{ kJ mol}^{-1}$, and $\sigma_P = 4.9 \times 10^3 \text{ MPa}$ [Goetze and Evans, 1979] (values are adjusted in accordance with the second invariants of stress and strain rate tensors). For diffusion and dislocation creep parameters, we use either the compilation made by Korenaga and Karato [2008] (hereinafter referred to as KK08) or that by Hirth and Kohlstedt [2003] (HK03). Because oceanic lithosphere is likely to be dehydrated upon its creation through mantle melting [Hirth and Kohlstedt, 1996; Evans et al., 2005], dry olivine rheology is considered, and recommended values according to KK08 are: $A_f = 1.78 \times 10^5 \text{ s}^{-1} \text{ MPa } \mu\text{m}^p$, $p = 2.98$, $E_f = 261 \text{ kJ mol}^{-1}$, $V_f = 6 \text{ cm}^3 \text{ mol}^{-1}$, $A_s = 1.23 \times 10^6 \text{ s}^{-1} \text{ MPa}^{-n}$, $n = 4.94$, $E_s = 610 \text{ kJ mol}^{-1}$, and $V_s = 13 \text{ cm}^3 \text{ mol}^{-1}$, whereas those by HK03 are: $A_f = 1.51 \times 10^9 \text{ s}^{-1} \text{ MPa } \mu\text{m}^p$, $p = 3$, $E_f = 357 \text{ kJ mol}^{-1}$, $V_f = 6 \text{ cm}^3 \text{ mol}^{-1}$, $A_s = 1.01 \times 10^5 \text{ s}^{-1} \text{ MPa}^{-n}$, $n = 3.5$, $E_s = 530 \text{ kJ mol}^{-1}$, and $V_s = 20.5 \text{ cm}^3 \text{ mol}^{-1}$. These preexponential factors assume that grain size is given in microns and σ_{II} in MPa. Grain size is assumed to be 10 mm [e.g., Ave Lallemand et al., 1980] for all of our calculations.

[14] For the yield stress criterion accompanying the above olivine rheology, we slightly modify equation (13) to

$$\tau_y = \frac{2\mu}{\sqrt{1 + \mu^2} - \mu} \rho_0 g z, \quad (26)$$

which corresponds to optimal thrust faulting [Turcotte and Schubert, 1982]. Though equation (13) is commonly used for pseudoplastic rheology, we choose to use the above equation, which describes a more accurate relation between the yield stress and the friction coefficient, to be in accord with the use of realistic mantle rheology. The effective viscosity for the plastic deformation is calculated by equation (19). For plate tectonic convection to take place, the (effective) friction coefficient μ need to be much lower than what laboratory experiments indicate [e.g., Moresi and Solomatov, 1998], and one way to achieve it is the thermal cracking of oceanic lithosphere [Korenaga, 2007]. Thermal cracking, however, cannot fracture the entire lithosphere, and the numerical modeling constrained by rock mechanical data indicates that cracking is possible where the temperature is below $\sim 700^\circ\text{C}$ [Korenaga, 2007]. Thus, we calculate the final pseudoplastic viscosity as

$$\eta^*(T^*, z^*) = \left(\frac{1}{\eta_y^*} + \frac{1}{\eta_{\text{ol}}^*} \right)^{-1}, \quad (27)$$

only when T is below a given threshold T_{max} , and use η_{ol}^* otherwise. Here all viscosities are normalized by η_r . Though we formulate the above rheology on the basis of the thermal cracking hypothesis, which is currently the only theory that provides a quantitative estimate on the depth extent of reduced friction, Stokes flow calculations themselves are not particularly restricted to this hypothesis, as we will test a range of T_{max} .

3. Numerical Results and Scaling Exponents

[15] Instantaneous Stokes flow is calculated with the 2-D finite element code of Korenaga and Jordan [2003], which

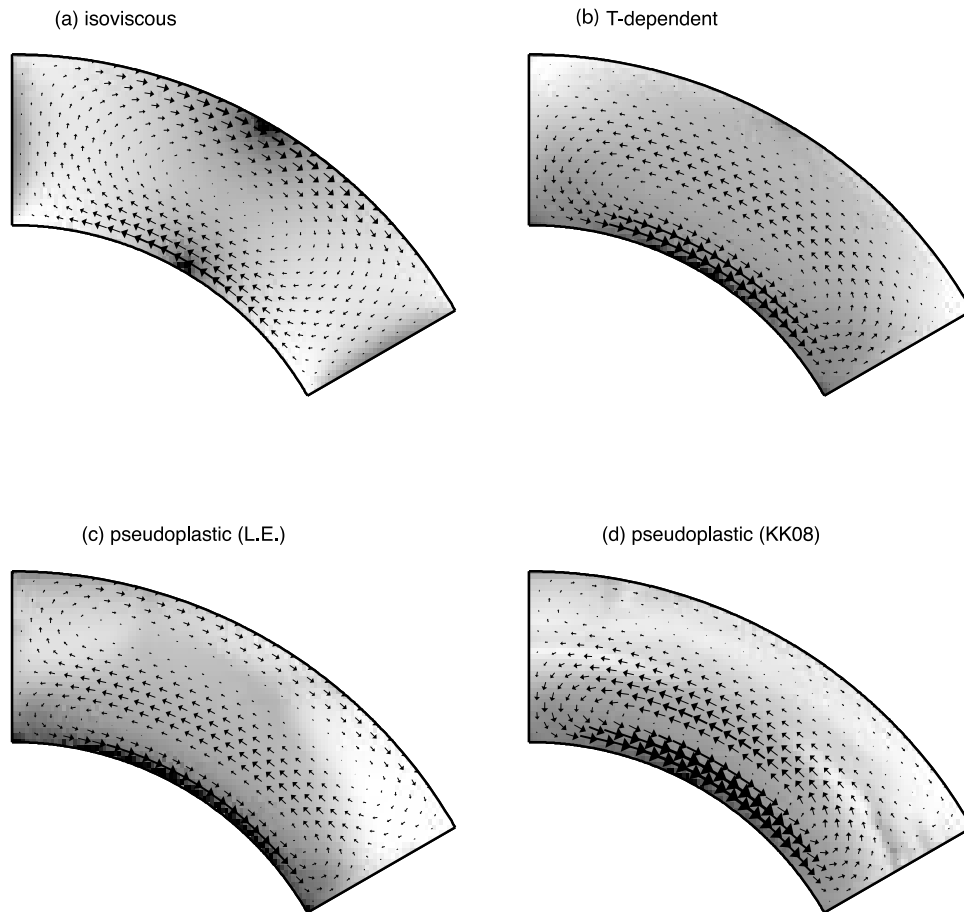


Figure 2. Examples of residual flow fields for (a) an isoviscous case, (b) a purely temperature-dependent viscosity case with $\theta = 10$, (c) a pseudoplastic rheology case (linear exponential) with $\theta = 20$ and $\gamma = 1$, and (d) a pseudoplastic olivine rheology case with KK08 flow laws, $\mu = 0.1$, and $T_{\max} = 700^\circ\text{C}$. In all cases, the dip angle is 60° , plate age is 100 Ma, the radius of curvature is 400 km, and plate velocity is 50 mm yr^{-1} . The scale of velocity arrows is the same. The magnitude of these residual fields is about 1/5–1/6 of the give plate velocity, so the total flow field is dominated by the angular flow field. Gray shading indicates the second invariant of stress (in the logarithmic scale); lighter shade indicates higher stress. The stress scale for shading varies for different cases.

has been modified for the polar coordinate system [cf. *Zhong and Gurnis, 1993*]. The model domain is discretized with 50×50 quadrilateral elements, using constant radial and angular increments. The benchmark test of the code was done with the analytical solution for Couette flow, and with this grid resolution, the RMS error of the velocity field is less than $10^{-3}\%$. For each type of rheology, we compute Stokes flow for all combinations of the following slab parameters: dip angle ϕ of 20° , 40° , 60° , and 80° , plate age t of 20, 60, 100, and 140 Ma, the radius of curvature R of 200, 300, 400, 500, and 600 km, and plate velocity v of 20, 40, 60, 80, and 100 mm yr^{-1} . For isoviscous and purely temperature dependent viscosity, we sample the parameter space more finely because the flow calculation does not require viscosity iteration. Bending dissipation is calculated as in equation (10) and dimensionalized with $\kappa = 10^{-6} \text{ m}^2 \text{ s}^{-1}$ and $\eta_r = 10^{19} \text{ Pa s}$.

3.1. Isoviscous Case

[16] An example of (residual) flow field is shown in Figure 2a, which is for the case with $\phi = 60^\circ$, $t = 100 \text{ Ma}$,

$R = 400 \text{ km}$, and $v = 50 \text{ mm yr}^{-1}$. Angular velocity with the magnitude of the given plate velocity is subtracted here to highlight bending deformation. For the first half of the subducting plate ($0 \leq \theta < 30^\circ$), the upper and bottom fractions are in extension and compression, respectively, so this part is bending, whereas an opposite sense of stress is observed for the second half of the plate ($30^\circ \leq \theta \leq 60^\circ$), which is unbending.

[17] Bending dissipation is shown in Figure 3 for some representative cross sections through the parameter space. We found that the functionality of bending dissipation can be described accurately by the following dipwise scaling relation:

$$\Phi_{\text{BD}}(t, R, v, \phi) = A(\phi)t^{\alpha_t}R^{\alpha_R}v^{\alpha_v}, \quad (28)$$

where t in Ma, R in km, v in mm yr^{-1} , and the scaling constant A as well as the exponents α_t , α_R , and α_v all depend on ϕ . The results of least squares fit are shown in Figure 4; misfit between calculated and predicted dissipation is $\sim 1\text{--}3\%$ for all dip angles (Figure 5a). The velocity exponent α_v is

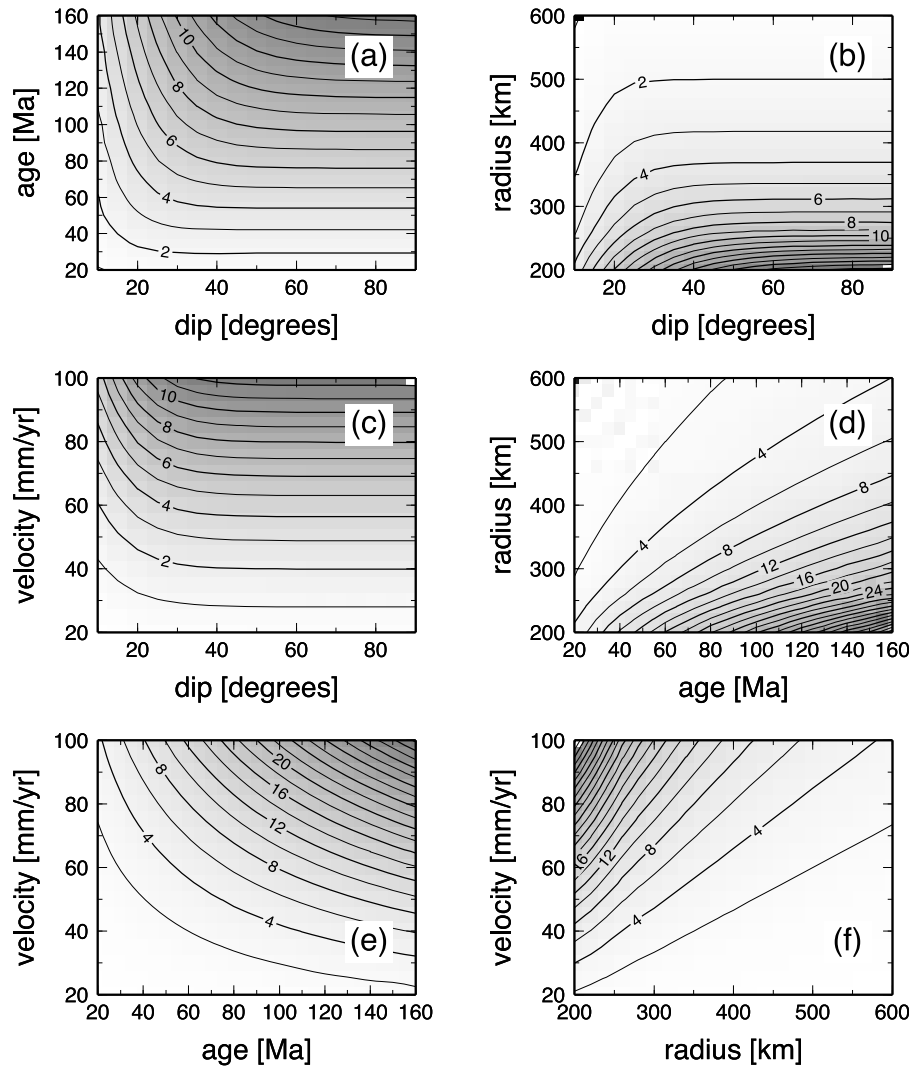


Figure 3. Bending dissipation (in W/m) with constant mantle viscosity ($\eta_r = 10^{19}$ Pa s) is shown for some representative cross sections: (a) dip vs. plate age, (b) dip vs. the radius of curvature, (c) dip vs. plate velocity, (d) age vs. the radius of curvature, (e) age vs. plate velocity, and (f) the radius of curvature vs. plate velocity. Slab parameters are fixed to the following values when they are not shown as coordinates: $\phi = 50^\circ$, $t = 60$ Ma, $R = 350$ km, and $v = 60$ mm yr $^{-1}$.

exactly 2 regardless of dip angle (Figure 4g), but other exponents exhibit interesting dip dependency (Figures 4c and 4e).

[18] Noting that $h \propto \sqrt{t}$ (equation (5)), the conventional scaling of equation (1) indicates $\alpha_t = 1.5$, $\alpha_R = -3$, and $\alpha_v = 2$. Our results suggest that there exists an important dip dependence, which is absent in this scaling, and that even at the limit of $\phi = 90^\circ$, the age and radius exponents do not converge to these conventional values. The origin of the conventional scaling is simple. It is based on the following approximation,

$$\Phi_{BD} = \int_S \eta e_{ij}^2 dS \sim \eta \left(\frac{vh}{R^2} \right)^2 (Rh), \quad (29)$$

where vh/R^2 is the scale for bending strain rate [Turcotte and Schubert, 1982] and Rh is the scale for the area of bending plate. The discrepancy between this dimensional analysis

and numerical results indicates that the (average) bending strain rate is not exactly proportional to h/R^2 , which is not surprising given the details of the deformation field (Figure 2a). As we will see in the following sections, this discrepancy from the conventional scaling further aggravates as we depart from constant viscosity.

[19] Note that models with different ages, dips, or radii have different domain sizes, and viscous dissipation calculated using equation (10) depends on the domain size. This is consistent to what is assumed in the conventional scaling (equation (29)), which is proportional to the area of bending plate.

3.2. Temperature-Dependent Viscosity

[20] The case of purely temperature-dependent viscosity was conducted by varying the Frank-Kamenetskii parameter θ from 2 to 20; the maximum θ corresponds to 317 kJ mol $^{-1}$ with $T_s = 273$ K and $\Delta T = 1300$ K. It is known that, for θ

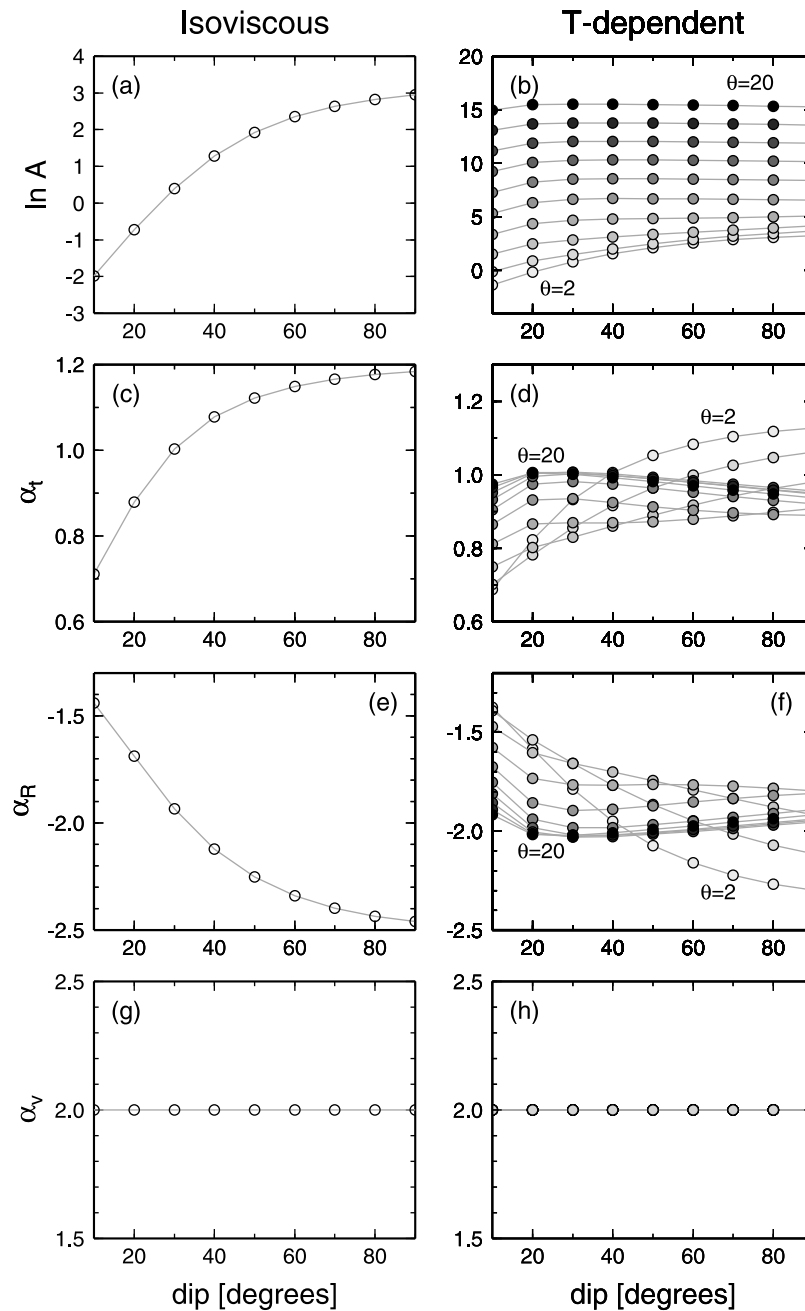


Figure 4. Results of dipwise linear regression for dissipation scaling (equation (28)) for the (left) isoviscous case and the (right) purely temperature-dependent case. (a-b) The natural logarithm of the scaling constant A , (c-d) the age exponent α_t , (e-f) the radius exponent α_R , and (g-h) the velocity exponent α_v , are shown as a function of dip angle. In the temperature-dependent case, darker shading corresponds to higher θ , which varies from 2 to 20. The velocity exponent was exactly 2 for all cases.

greater than ~ 10 , the viscosity contrast in the system is so large that the mode of convection becomes stagnant lid [Solomatov, 1995], so the scaling derived for this rheology is not expected to be useful for studying bending dissipation in plate tectonics. Our reason to consider purely temperature-dependent viscosity here is merely to provide a point of reference when discussing more complex rheology, in which additional weakening mechanism is included.

[21] For each value of θ , we conduct dipwise least squares regression as for the isoviscous case, and results are shown

in Figure 4. The fit between input data and prediction is again excellent (Figure 5b). As in the isoviscous case, the velocity exponent α_v is exactly 2 for all cases considered (Figure 4h). As θ increases, the age exponent α_t and radius exponent α_R become nearly independent of dip angle and appear to converge to 1 and -2 , respectively (Figures 4d and 4f). That is, bending dissipation becomes less sensitive to plate thickness and the radius of curvature as temperature dependency increases. This is because the top portion of the plate is so stiff to deform that bending deformation is

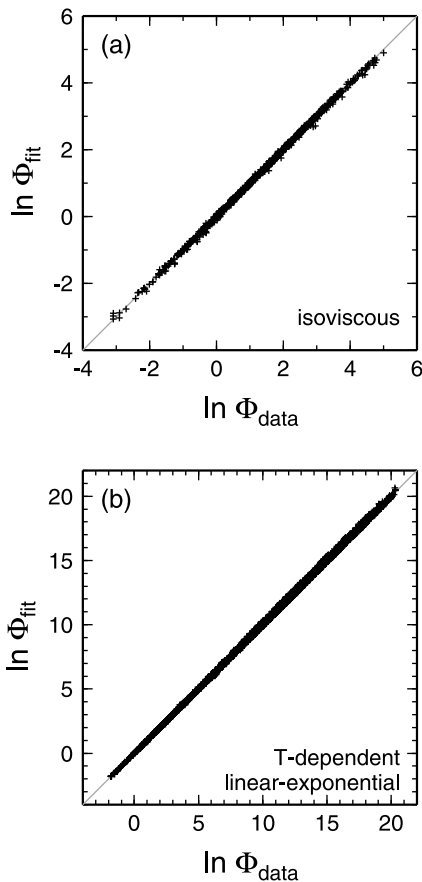


Figure 5. Comparison in the logarithmic scale of predicted bending dissipation based on estimated scaling, Φ_{fit} , with original values, Φ_{data} , for (a) the isoviscous case (section 3.1) and (b) the purely temperature-dependent case (section 3.2).

restricted to the lower portion (Figure 2b), effectively reducing both plate thickness and the radius of curvature. Also, the upper half of the plate is supposed to move faster than the median plane (see Figure 2a), but such excess in velocity is suppressed by the stiff top, which moves with the given plate velocity. In the first half of the plate ($0 \leq \theta < 30^\circ$), this suppression is equivalent to the compression of the upper fraction, which is offset by the extension of the bottom part. Unlike the isoviscous case, therefore, the subducting plate experiences unbending first, followed by bending.

3.3. Pseudoplastic Rheology

[22] We first used the linear exponential temperature-dependent viscosity (equation (11)) for pseudoplastic viscosity, and Stokes flow was calculated for all the combinations of $\theta = 10, 15, 20, 25,$ and 30 and $\gamma = 0.25, 0.5, 1.0, 1.25, 1.5,$ and 2.0 . With $\alpha = 3 \times 10^{-5} \text{ K}^{-1}$ and $\Delta T = 1300 \text{ K}$, for example, γ of 1.0 corresponds to the friction coefficient μ of 0.04, so these values for γ correspond to very low effective friction coefficients. To simulate plate tectonic convection with pseudoplastic rheology and realistically high θ , γ has to be in this low regime [Korenaga, 2010].

[23] The results of dipwise linear regression for dissipation scaling are shown in Figure 6. The fit between input data and prediction is not as good as in the earlier cases (Figure 7a), but the overall RMS error is only 1.3%,

meaning that the vast majority of dissipation calculations are well predicted by the fitted scaling. The effect of varying γ is confined mostly to the scaling constant A ; greater γ naturally gives rise to greater dissipation. As in the case of purely temperature-dependent viscosity, the scaling exponents are not very sensitive to dip angle when $\theta \geq \sim 15$ (Figures 6c, 6e, and 6g). The age exponent is ~ 1 for all cases, and excluding the cases with θ of 10, the radius exponent is ~ -0.5 , and the velocity exponent is ~ 1.2 . Compared to the conventional scaling (equation (1)), therefore, all exponents are reduced, most notably the radius exponent.

[24] The reduced velocity exponent is most likely due to stress-dependent rheology; greater plate velocity would lead to greater stresses, which in turn reduce viscosity and thus stresses, and this negative feedback results in a weaker sensitivity to plate velocity. The origin of other reduced sensitivities may be found in the residual velocity field (Figure 2c). Unlike the case of the purely temperature-dependent viscosity (Figure 2b), the top fraction of the plate can deform due to pseudoplasticity, and it experiences first extension and then compression as in the isoviscous case. What happens below is, however, more complex than in the isoviscous case. There exist two neutral planes virtually free of bending deformation, one above and one below the median plane, and the upper half of the plate undergo bending and then unbending whereas the lower half experiences the opposite. This is because, with pseudoplastic rheology, the plate is strongest in the middle, so the the upper and lower parts resemble, respectively, the isoviscous case and the purely temperature-dependent case. This divided flow pattern reduces the length scale for bending deformation as well as its velocity scale, so dissipation becomes less sensitive to plate thickness (i.e., age) and the radius of curvature.

[25] We also use the temperature-dependent viscosity of the Arrhenius form (equation (21)) by using the activation energy E corresponding to θ used in the above with $T_s = 273 \text{ K}$ and $\Delta T = 1300 \text{ K}$, to facilitate one-to-one comparison. Results for scaling exponents are summarized in Figure 6, and there is no major difference from the case of linear exponential viscosity. Even the case of $\theta = 10$ ($E = 158 \text{ kJ mol}^{-1}$) behaves similarly to those with higher θ , because the total viscosity contrast is greater for the Arrhenius form if compared at the same θ .

[26] In addition to viscous dissipation, the effective viscosity contrast is also calculated as [Parmentier *et al.*, 1976]

$$\Delta\eta = \frac{\eta_{\text{eff}}}{\eta_r} = \frac{\int_S \eta^*(e_{ij}^*)^2 dS}{\int_S (e_{ij}^*)^2 dS}, \quad (30)$$

and the viscosity contrasts for the linear exponential and Arrhenius cases are compared in Figure 8. The majority of cases have the difference between these cases less than a factor of 3. This is expected because pseudoplasticity limits the difference of total viscosity contrasts [e.g., Solomatov, 2004].

3.4. Pseudoplastic Olivine Rheology

[27] For the pseudoplastic rheology with olivine flow laws, we used all the combinations of $\mu = 0.05, 0.1, 0.2, 0.4,$ and 0.8 and $T_{\text{max}} = 350^\circ\text{C}, 700^\circ\text{C},$ and 1300°C , for both KK08 and HK03 compilations. The scaling exponents

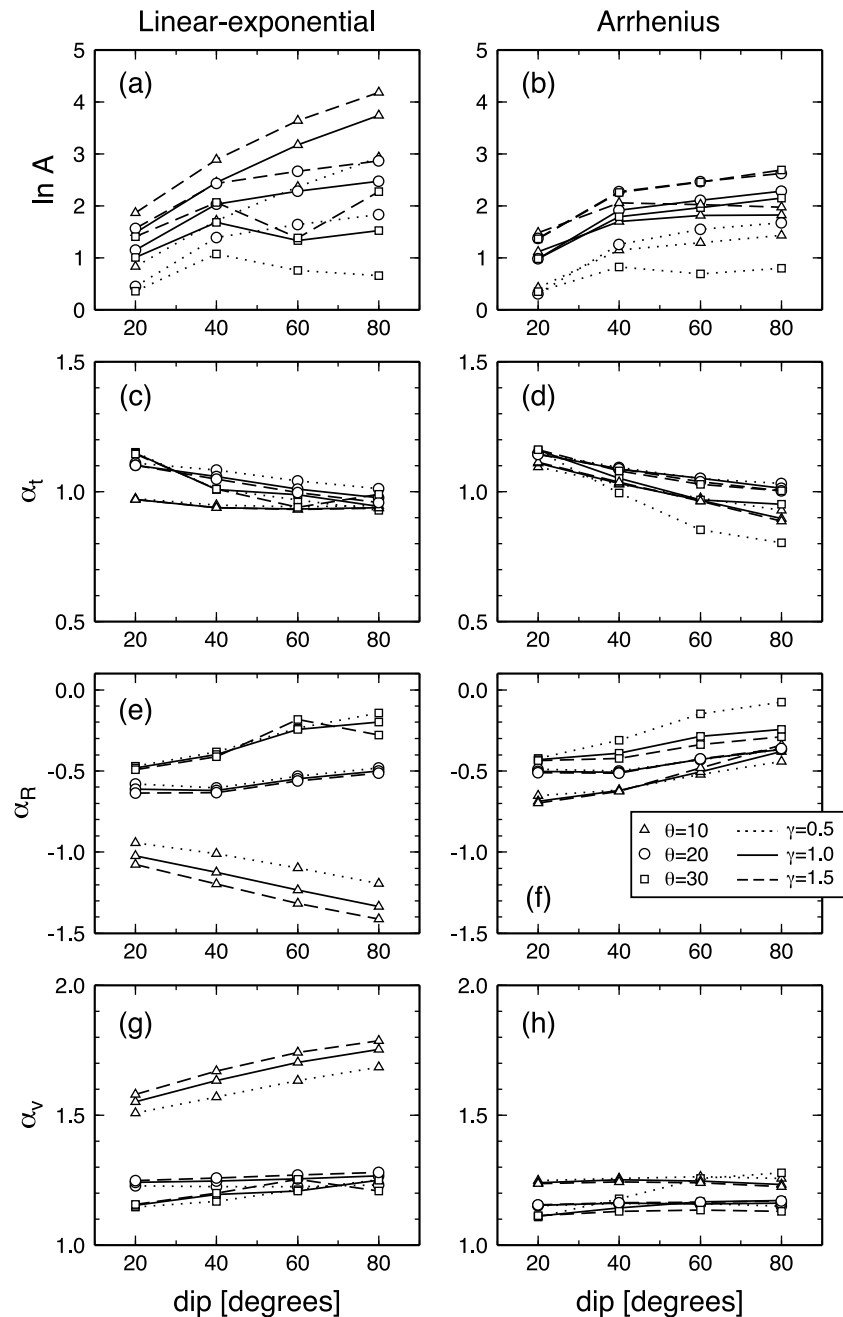


Figure 6. Same as Figure 4, but for pseudoplastic rheology with temperature-dependent viscosity of the (left) linear exponential form and the (right) Arrhenius form. Results are shown for the combination of the following values: $\theta = 10$ (triangles), 20 (circles), and 30 (squares), and $\gamma = 0.5$ (dotted), 1.0 (solid), and 1.5 (dashed).

estimated by linear regression are summarized in Figure 9. No major difference can be seen between KK08 and HK03, except that HK03 tends to result in greater effective viscosity up to a factor of ~ 10 (Figure 10a). The pattern of the residual velocity field is similar to the simpler version of pseudoplastic rheology (Figure 2d). The age and velocity exponents are also similar to those estimated for simple pseudoplastic rheology, but the radius exponent exhibits intriguing dip dependency (Figures 9e and 9f), and it has to do with the pressure dependency of olivine rheology, which is probably the most important difference from the simpler

pseudoplastic rheology. For $T_{\max} \geq 700^\circ\text{C}$, the radius component can become positive for larger dip angles; i.e., bending dissipation may be greater for the larger radius of curvature when the subducting slab is steeply dipping. This counterintuitive behavior takes place only when the friction coefficient is not too low ($\geq \sim 0.4$), implying that olivine rheology is the primary cause. A larger radius of curvature for a steeply dipping slab means that bending deformation takes place over a greater depth range, and because of the pressure-dependent viscosity (due to nonzero activation

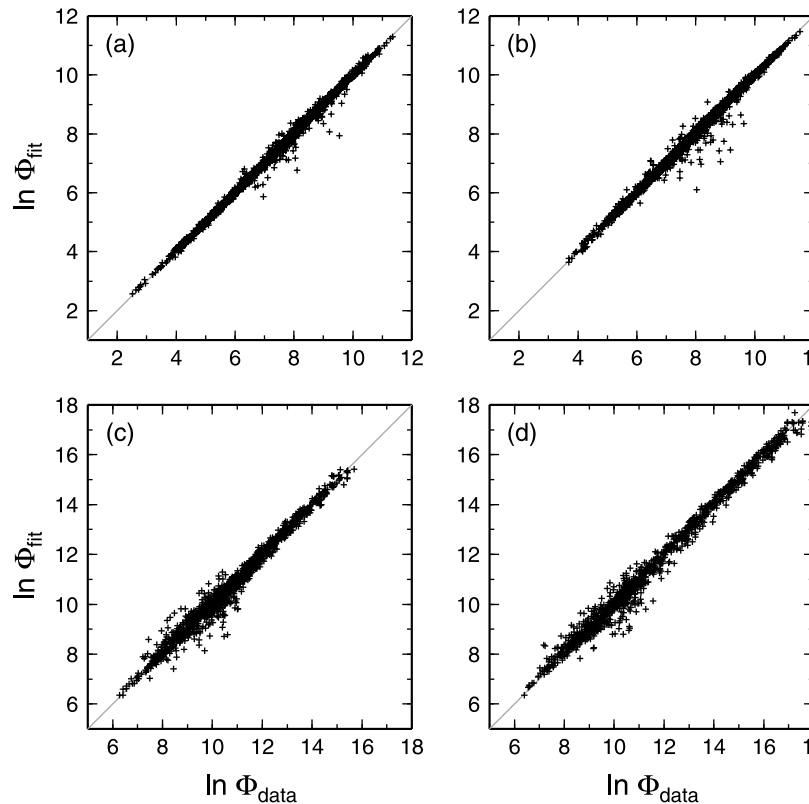


Figure 7. Same as Figure 5, but for pseudoplastic rheology with (a) linear exponential temperature-dependent viscosity, (b) Arrhenius temperature-dependent viscosity, (c) KK08 olivine flow laws, and (d) HK03 olivine flow laws. Overall RMS errors of prediction (measured in the logarithmic scale) are 1.3% (Figure 7a), 1.5% (Figure 7b), 20.8% (Figure 7c), and 2.9% (Figure 7d).

volume), deformation at greater depths involves greater viscous dissipation.

[28] When $T_{\max} = 350^{\circ}\text{C}$, viscous dissipation is considerably high regardless of the friction coefficient (Figures 9a and 9b). Thus, if thermal cracking does not penetrate as deeply as suggested by *Korenaga* [2007], it would not be able to weaken oceanic lithosphere sufficiently. The exponents for the cases with the low T_{\max} indeed resemble closely that for the strongly temperature-dependent viscosity (e.g., $\alpha_R \sim -2$). On the other hand, the cases with $T_{\max} = 700^{\circ}\text{C}$ are very similar to those with $T_{\max} = 1300^{\circ}\text{C}$, indicating that cracking down to the isotherm of 700°C is almost as effective as damaging the entire lithosphere by fracturing.

[29] When $T_{\max} \geq 700^{\circ}\text{C}$, effective lithospheric viscosity calculated from equation (30) is on the order of 10^{21} to 10^{23} for strain rates appropriate for plate bending, i.e., $\sim 10^{-14} \text{ s}^{-1}$ (Figure 10b). Because bending dissipation is linearly proportional to the effective viscosity, it may be understood that bending dissipation can be easily modified by an order of magnitude by varying the slab parameters within their plausible ranges, and by greater magnitudes by varying mantle rheology.

4. Discussion

4.1. Effects of Boundary Conditions

[30] Our modeling strategy in this study is to focus on the bending deformation of plates at subduction zones, using the

minimum model domain (Figure 1). As for any regional or local flow models, however, boundary conditions are all artificial. As described in section 2.1, the slab top is free slip to approximate low frictional resistance along the slab surface, and the slab bottom is also free slip to approximate low viscous stresses owing to the weak asthenosphere. Constant

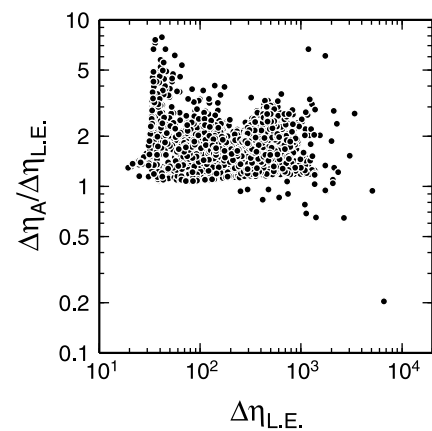


Figure 8. Effective viscosity contrasts for pseudoplastic rheology are compared for the two different forms of temperature dependency. The one for the Arrhenius form $\Delta\eta_A$ is generally higher than that for the linear exponential form $\Delta\eta_{L.E.}$, mostly up to a factor of 3.

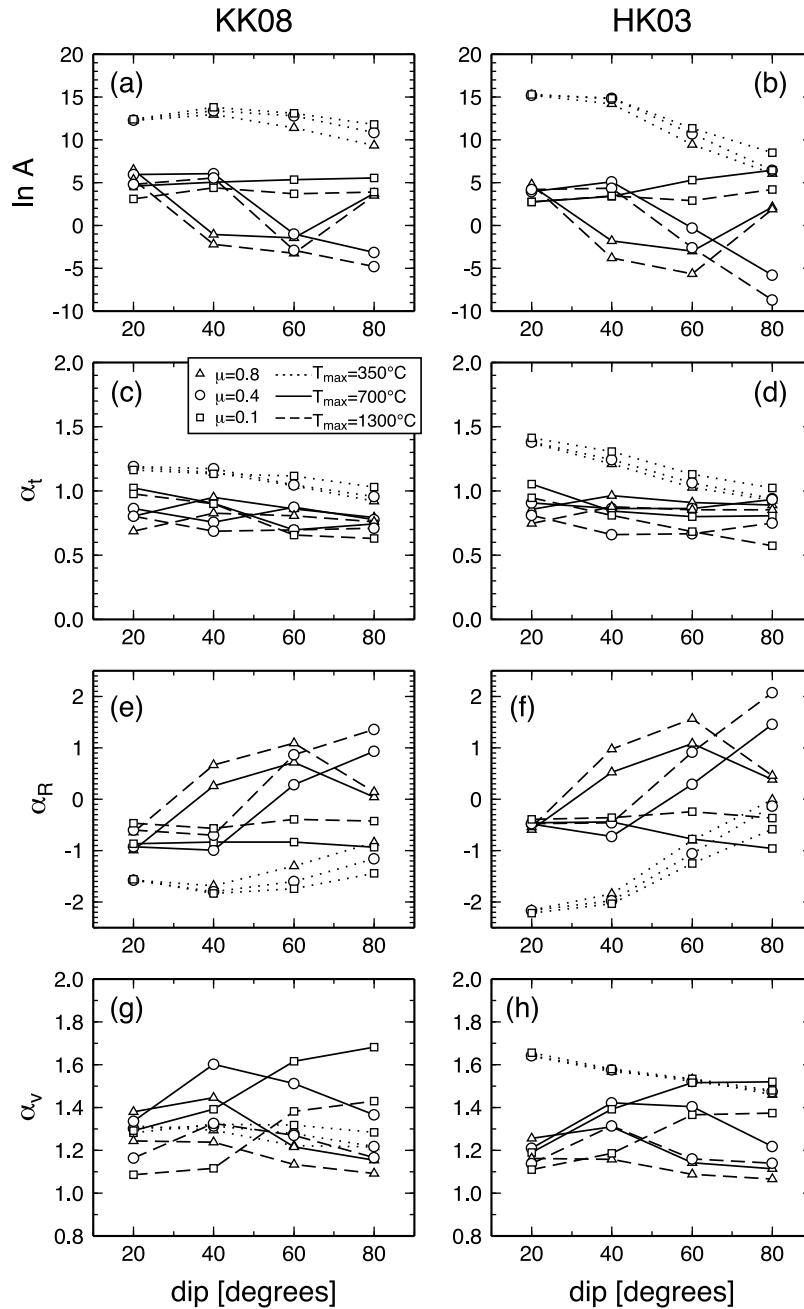


Figure 9. Same as Figure 4, but for pseudoplastic rheology with olivine flow laws based on (left) KK08 compilation and (right) HK03 compilation. Results are shown for the combination of the following values: $\mu = 0.8$ (triangles), 0.4 (circles), and 0.1 (squares), and $T_{max} = 350^\circ\text{C}$ (dotted), 700°C (solid), and 1300°C (dashed).

angular velocity is used at the inflow and outflow boundaries to make the model symmetric, and such simplicity is important for scaling analysis. Note that this simple situation is also assumed in the conventional scaling of equation (1) [e.g., *Conrad and Hager, 1999*]. In a real bending plate, however, the outflow velocity does not need to be identical to the inflow velocity, and there may also be nonzero radial velocity components if, for example, a slab is retreating. Taking into account all of these realistic complications in a systematic manner defies the purpose of our simple scaling analysis, because it would result in a nontrivial increase in

the dimension of the parameter space, which in turn implies at least a few orders of magnitude more flow calculations. Nonetheless, it is still important to examine the effects of the chosen boundary conditions by relaxing them with a bigger model domain. To this end, we conducted additional flow calculations by extending the model domain in both the along- and across-the-slab directions (Figure 11).

[31] The original model domain is extended radially by 20%, and the new model domain also contains straight segments attached to the bending part, each of which is half as long as the original domain. As the polar coordinate

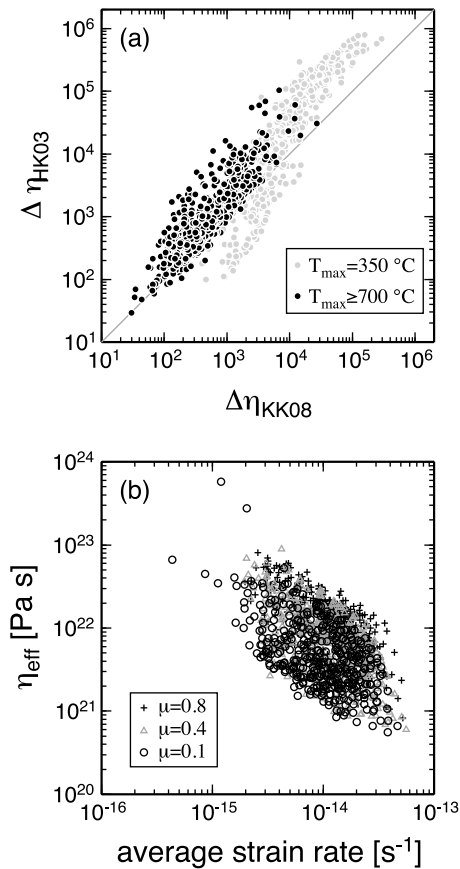


Figure 10. (a) Effective viscosity contrasts for pseudoplastic olivine rheology are compared for the cases with KK08 and HK03 compilations. Gray circles are for the cases with $T_{max} = 350^\circ\text{C}$, and solid circles for higher T_{max} . (b) Effective viscosity (for KK08) is shown as a function of average bending strain rate for the cases of $T_{max} = 700^\circ\text{C}$ with $\mu = 0.8$ (crosses), 0.4 (triangles), and 0.1 (circles).

system is no longer appropriate, the Cartesian version of the finite element code was used. The employed boundary conditions are as follows. The top and bottom boundaries are assigned zero velocity (i.e., no slip), and the inflow and outflow boundaries have the constant plate velocity. To simulate low frictional stresses along the slab top, the model fraction located above the original model top is assigned with a low viscosity ($\eta^* = 10^{-5}$). The temperature field below this weak zone is prescribed by equation (4), so the model fraction located below the original model bottom corresponds to the hotter, asthenospheric mantle. We repeated instantaneous Stokes flow calculations with this extended model domain for the cases of pseudoplastic rheology with linear exponential temperature-dependent viscosity and with the KK08 olivine flow law. In these cases, the asthenospheric viscosity (i.e., the viscosity below the original model bottom) is much lower than the lithospheric viscosity, so low viscous stresses are expected along the slab bottom.

[32] An example of the residual velocity field is shown in Figure 11b for the case of pseudoplastic rheology with the KK08 flow law. Though details differ most notably by radial velocity components, the gross characteristics of the

velocity field remain the same in the original model domain (see Figure 2d); there are two neutral planes with little bending deformation, one above and one below the median plane, and the upper half of the plate undergoes bending and then unbending whereas the lower half experiences the opposite. As suggested in section 3.3, this is probably because the strength of plate is greatest in the middle; the upper plate is weaker because of lower pressure (i.e., lower frictional resistance), and the lower plate is weaker because of higher temperature (i.e., lower viscosity). This vertical stratification of plate strength results in the split pattern of the bending deformation field. The residual velocity field

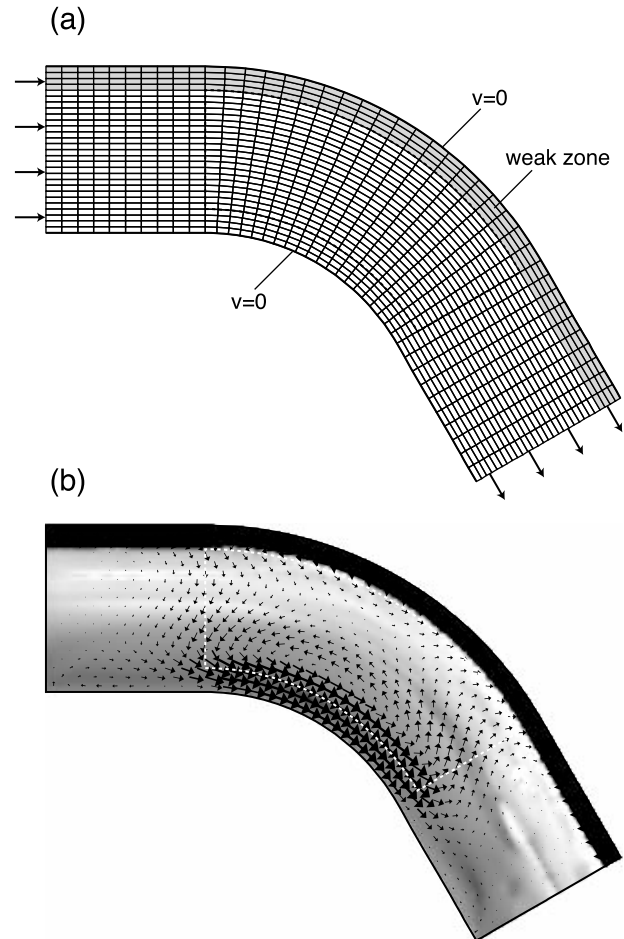


Figure 11. (a) Finite element discretization of an extended model domain and (b) residual flow field, for a pseudoplastic olivine rheology case with KK08 flow laws, $\mu = 0.1$, and $T_{max} = 700^\circ\text{C}$. As in Figure 2, the dip angle is 60° , plate age is 100 Ma, the radius of curvature is 400 km, and plate velocity is 50 mm yr^{-1} . The region enclosed by dashed line corresponds to the original model domain. While a flow field is computed in the extended domain, viscous dissipation is still integrated only in the original domain to make a comparison with the original scaling straightforward. In Figure 11a, shaded elements denote a weak zone with a prescribed viscosity of $\eta^* = 10^{-5}$. In Figure 11b, gray shading indicates the second invariant of stress (in the logarithmic scale); lighter shade indicates higher stress. The weak zone is characterized by vanishingly small stresses.

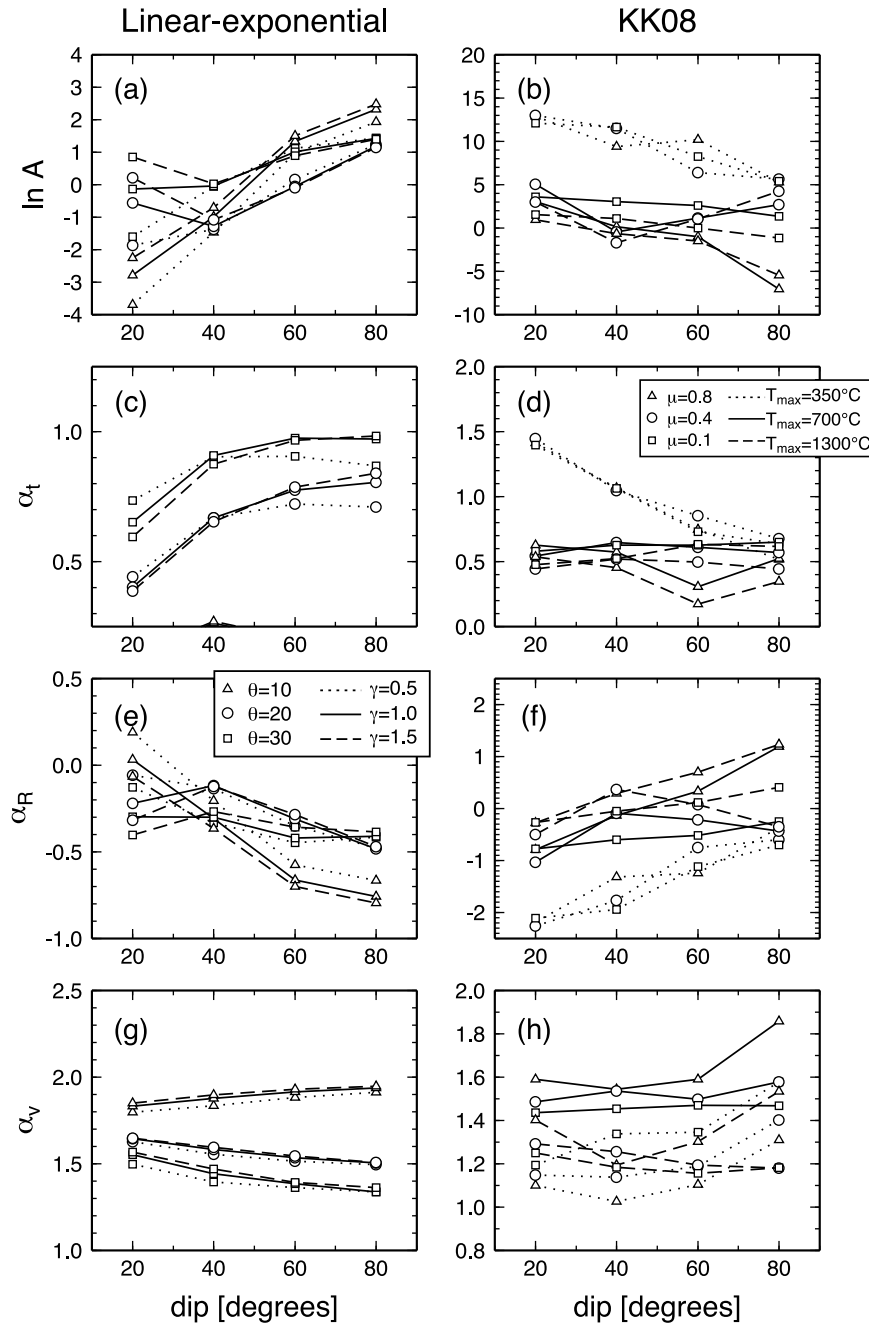


Figure 12. Results of dipwise linear regression for dissipation scaling (equation (28)) using flow calculations with the extended model domain (note that viscous dissipation is still calculated for the original model domain as indicated by dashed lines in Figure 11), for pseudoplastic rheology with temperature-dependent viscosity of the (left) linear exponential form and for (right) pseudoplastic rheology with KK08 olivine flow laws.

decays rapidly in the straight portions of the extended model, suggesting that the essence of bending deformation is captured reasonably well by the original model. The same sets of Stokes flow calculations with a range of slab and rheology parameters (as done in sections 3.3 and 3.4) were conducted, and viscous dissipation within the original model domain was calculated. The results of dipwise linear regression for dissipation scaling are summarized in Figure 12. The

details of dipwise behavior are different from the original results, but more important is that all of exponents are reduced compared to their conventional values ($\alpha_t = 1.5$, $\alpha_R = -3$, and $\alpha_v = 2$), and the radius exponent is found to be positive in some cases, thereby substantiating the original finding. Our original finding is based on the minimum model domain for bending with the simplest boundary conditions, so it will be

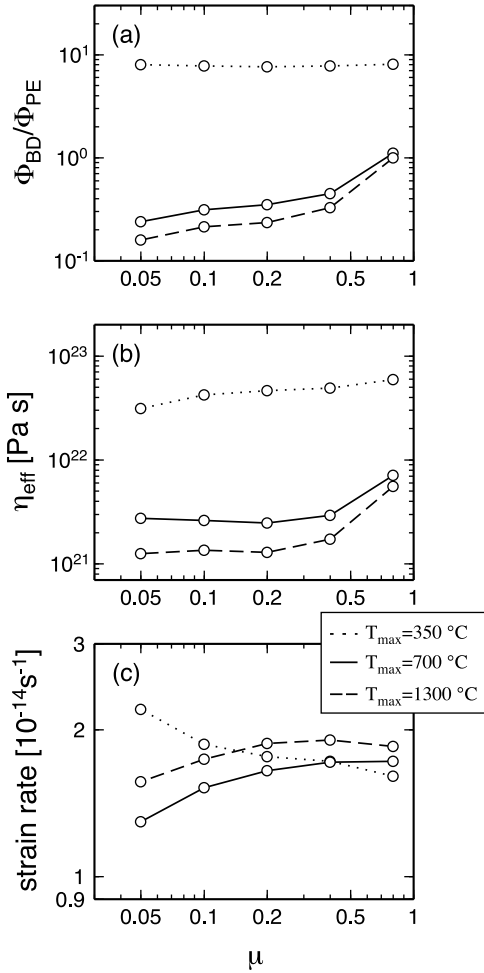


Figure 13. Estimates on global bending dissipation using pseudoplastic olivine rheology with KK08 flow laws. (a) The ratio of bending dissipation over potential energy release, (b) effective lithospheric viscosity, and (c) average bending strain rate are shown as a function of μ , for the cases of $T_{max} = 350^\circ\text{C}$ (dotted), 700°C (solid), and 1300°C (dashed).

useful as a reference when quantifying the effects of realistic deviations from the assumed boundary conditions.

4.2. Rate of Viscous Dissipation and Potential Energy Release

[33] *Lallemand et al.* [2005] and *Wu et al.* [2008] have published tables of all the subduction zones currently active on Earth and their various geometries. Using the parameters from these tables and assuming pseudoplastic olivine rheology, we can estimate the rates of global bending dissipation and global potential energy release. Some of relevant entries in their tables were left unfilled due to insufficient data. For our global estimates, we filled these entries as follows: (1) if there were adjacent subduction zones with well constrained parameters, we used those values, and (2) if there were no such neighbors, we used global average values. Appendix A lists the full table of results for worldwide subduction zones.

[34] The rate of gravitational potential energy release for the slab geometry shown in Figure 1 can easily be derived as [cf. *Turcotte and Schubert*, 1982]:

$$\Phi_{PE}(t, R, v, \phi, L) = \Phi_{PE,1} + \Phi_{PE,2}$$

$$= 2\rho_0\alpha g\Delta TLv \sin\phi\sqrt{\kappa t} \int_0^\beta \operatorname{erfc}(u) du \quad (31)$$

$$+ 4\rho_0\alpha g\Delta Tv(1 - \cos\phi)\kappa t \int_0^\beta \operatorname{erfc}(u) \left(\frac{R}{2\sqrt{\kappa t}} - u\right) du, \quad (32)$$

where $\Phi_{PE,1}$ and $\Phi_{PE,2}$ correspond to the straight and bending portions of the subducting plate, respectively, and $\beta = \operatorname{erf}^{-1}(0.9)$. This is the energy release per unit length, so by multiplying with the width of a subduction zone, we can calculate the energy release from each subduction zone. Contributions from the all subduction zones add up to ~ 3.2 TW. To estimate the rate of bending dissipation, we use the pseudoplastic rheology with the KK08 compilation and calculate Stokes flow for each subduction zone. The global energy balance requires that bending dissipation must be smaller than potential energy release, and it is certainly possible to satisfy this requirement if $T_{max} \geq 700^\circ\text{C}$ and $\mu < 0.8$ (Figure 13a). With $T_{max} = 700^\circ\text{C}$, global bending dissipation is $\sim 50\%$ of global energy release for $\mu = 0.4$ and $\sim 30\%$ for $\mu = 0.1$. Corresponding lithospheric viscosity is $\sim 3 \times 10^{21}$ Pa s, which does not depend strongly on μ (Figure 13b). These estimates on bending dissipation bear little significance because the actual weakening mechanism that compensates strongly temperature-dependent viscosity is still very uncertain. It should be clear by now, however, that the role of bending dissipation in global energy balance depends critically on the details of mantle rheology. One can always define effective lithospheric viscosity, but as we saw in the previous sections, how bending dissipation scales with various slab parameters is sensitive to the functionality of mantle rheology.

4.3. Parameterization of Effective Lithospheric Viscosity

[35] This study is based on Stokes flow calculations with kinematic boundary conditions, in which an imposed plate velocity is not necessarily consistent with other slab parameters; for example, a young plate with a low dip angle would not subduct quickly. As mentioned in section 2.1, however, the lack of dynamical consistency is not an issue for the scaling of bending dissipation, and the derived scaling is useful when analyzing the results of fully dynamic models. Such application of the scaling is attempted in this section.

[36] Based on a series of convection modeling with the pseudoplastic rheology defined by equations (11) and (20), *Korenaga* [2010] derived the following heat flow scaling:

$$Nu = 2 \left(\frac{Ra_i}{Ra_c}\right)^{1/3} \Delta\eta_L^{-1/3}, \quad (33)$$

and the velocity scaling:

$$\frac{v}{\kappa/D} = 4 \left(\frac{L}{D}\right) \left(\frac{Ra_i}{Ra_c}\right)^{2/3} \Delta\eta_L^{-2/3}, \quad (34)$$

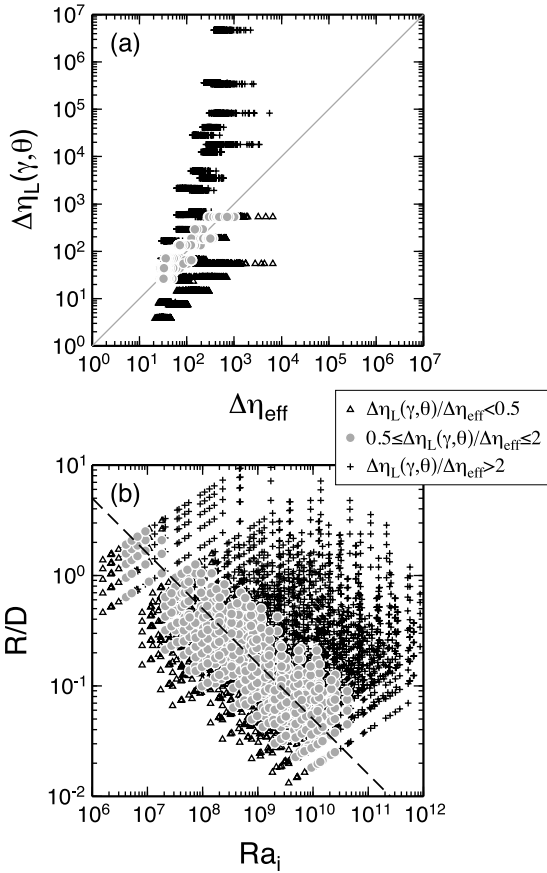


Figure 14. (a) Comparison of effective viscosity contrast based on Stokes flow calculations with pseudoplastic rheology, $\Delta\eta_{\text{eff}}$, with prediction from the parameterization of *Korenaga* [2010], $\Delta\eta_L(\gamma, \theta)$. (b) Covariation of non-dimensionalized radius of curvature, R/D , and the internal Rayleigh number, Ra_i . Dashed line represents $R/D \propto Ra_i^{-1/2}$. Different symbols denote the following three cases: $\Delta\eta_L(\gamma, \theta)/\Delta\eta_{\text{eff}} < 0.5$ (triangles), $0.5 \leq \Delta\eta_L(\gamma, \theta)/\Delta\eta_{\text{eff}} \leq 2$ (circles), and $\Delta\eta_L(\gamma, \theta)/\Delta\eta_{\text{eff}} > 2$ (crosses).

where Nu is the Nusselt number, Ra_i is the internal Rayleigh number, Ra_c is the critical Rayleigh number (set to 10^3), D is the depth of the convection system, L/D is the average aspect ratio of convection cells, and $\Delta\eta_L$ is the effective lithospheric viscosity contrast. Using the notation in this paper, the internal Rayleigh number may be defined as

$$Ra_i = \frac{\alpha\rho g\Delta TD^3}{\kappa\eta_r} = Ra_R \left(\frac{D}{R}\right)^3. \quad (35)$$

The effective viscosity contrast was found to have the following functionality:

$$\Delta\eta_L(\gamma, \theta) \approx \exp(0.327\gamma^{0.647}\theta), \quad (36)$$

that is, the viscosity contrast is determined entirely by the two rheological parameters.

[37] Effective viscosity contrasts from our plate bending calculation with exactly the same formulation of pseudoplastic rheology (section 3.3), however, depend also on slab

parameters, and these two types of viscosity contrasts do not agree well (Figure 14a); equation (36) overpredicts the viscosity contrast for many cases. This discrepancy itself is not surprising; our Stokes flow calculations are driven by kinematic boundary conditions whereas the convection model of *Korenaga* [2010] is dynamically self-consistent so that the effective lithospheric viscosity is internally regulated. Our intent here is to make use of both studies to better understand the origin of the empirical viscosity scaling of equation (36). In this section, we limit ourselves to numerical results for the maximum dip angle used ($\phi = 80^\circ$), because convection simulation usually exhibits $\phi \sim 90^\circ$.

[38] Using the following approximate relation between the Nusselt number and plate thickness at a subduction zone (i.e., maximum plate thickness),

$$2Nu^{-1} \approx \frac{h}{D} = \left(\frac{h}{R}\right)\left(\frac{R}{D}\right), \quad (37)$$

the heat flow scaling of equation (33) may be rearranged as

$$Ra_R = \left(\frac{R}{h}\right)^3 \Delta\eta_L(\gamma, \theta) Ra_c. \quad (38)$$

Similarly, the velocity scaling (equation (34)) can be used to derive

$$\left(\frac{R}{D}\right) = 4\Delta\eta_L(\gamma, \theta)^{-1/2} \left(\frac{Ra_R}{Ra_c}\right)^{2/3} \left(\frac{\kappa}{vR}\right), \quad (39)$$

for which we assume $L/D \sim \Delta\eta_L^{1/6}$ [*Korenaga*, 2010]. The internal Rayleigh number Ra_i can then be calculated from Ra_R and R/D (equation (35)). For all combinations of plate thickness, the radius of curvature, and plate velocity, we can derive the corresponding pairs of R/D and Ra_i (Figure 14b), and the condition that $\Delta\eta_{\text{eff}} \approx \Delta\eta_L(\gamma, \theta)$ delineates the following trend,

$$\left(\frac{R}{D}\right) \propto Ra_i^{-1/2}. \quad (40)$$

We thus suggest that the viscosity scaling of equation (36) is likely a consequence of this self-regulation of the convective flow field.

[39] The above scaling for the radius of curvature is, however, different from what suggested by *Korenaga* [2010], in which the exponent is $-1/6$ instead of $-1/2$. There are at least two reasons for this discrepancy. First, the derivation of *Korenaga* [2010] is based on stress balance regarding the transition from plate tectonic convection to stagnant lid convection, so convection away from this transition may exhibit different scaling. Second, his derivation assumes the conventional scaling of bending strain rate (section 3.1), which is clearly invalid for pseudoplastic rheology as suggested by the previous sections. The self-organization of thermal convection with highly nonlinear rheology is an interesting subject that warrants future research efforts.

4.4. Some Remarks on Previous Studies

[40] Most of recent studies that concern bending dissipation are based on free subduction models [e.g., *Bellahsen*

et al., 2005; *Stegman et al.*, 2006; *Capitanio et al.*, 2007, 2009; *Schellart*, 2009], in which a plate is let fall down by its own negative buoyancy, and the viscosity of plate is usually set to be constant or Newtonian. Although studying a simple dynamical system has its own merit, our finding on the scaling of plate bending indicates that the use of Newtonian rheology limits the applicability of their studies to actual subduction zones on Earth. Notable exceptions are the models of *Stegman et al.* [2006] and *Di Giuseppe et al.* [2008], in which pseudoplastic rheology was employed, but these studies combined constant lithospheric viscosity with yield stress-based viscosity, and the strong temperature dependency of mantle rheology was not considered.

[41] The work of *Krien and Fleitout* [2008] is based on calculating instantaneous Stokes flow with an elaborate rheological model, which contains both lateral and vertical viscosity variations in the sublithospheric mantle, but the rheology of oceanic lithosphere is either constant viscosity or power law rheology with a high stress exponent ($n = 10$). Our study suggests that the former is inadequate whereas the validity of the latter remains unclear. They tried to discriminate different models by comparing with geoid and gravity signatures over subduction zones, but inference on mantle rheology from surface observables is generally highly nonunique. Nonuniqueness may be reduced by limiting the functionality of rheology, but when doing so, care must be taken so that the realistic behavior of mantle rheology can still be captured by such limited functionality. *Wu et al.* [2008] estimated the viscosity of bending plate by comparing predicted global plate motion with the observed one, but their calculation of global plate motion is based on the conventional scaling of bending dissipation (equation (1)). More recently, *Leng and Zhong* [2010] argued that the bending dissipation accounts for only 10–20% of the total dissipation based on compressible convection models with temperature-dependent viscosity, but the temperature dependency they used is too weak ($\theta \sim 11$) to approximate mantle rheology. It is known that such convection does not exhibit plate-like behaviors [e.g., *Bercovici et al.*, 2000]. To simulate more plate-like surface motions, therefore, they also tried models that includes prescribed weak zones, and what they were able to achieve is essentially the same as what we have done with purely temperature-dependent viscosity with low θ (section 3.2 and Figure 4). Though the ‘effective’ activation energy of temperature-dependent viscosity may be lower than what high-temperature creep mechanisms indicate if other low-temperature deformation mechanisms are taken into account, our results suggest that one cannot emulate such effect by simply using weakly temperature-dependent viscosity, as far as the scaling of bending dissipation is concerned (compare, for example, Figures 4b, 4d, 4f, and 4h with Figures 9a, 9c, 9e, and 9g).

[42] The use of the effective viscosity (as defined in equation (30)) when evaluating bending dissipation may be traced back to the work of *Conrad and Hager* [1999]. In their numerical experiments, both temperature-dependent and stress-dependent rheology were used (though yielding was not included), and their results were found to be insensitive to the particular form of rheology if parameterized in terms of the effective viscosity. The temperature-dependent viscosity they used is of the Arrhenius form

(equation (21)), but the viscosity was cut off at the maximum contrast of 10^4 . This is close to the case of purely temperature-dependent viscosity with low θ , and in this case, our results suggest that the velocity exponent takes a conventional value of 2.0, and the age exponent is also similar to its conventional value (Figures 4d and 4h). Furthermore, the radius curvature and the dip angle were fixed to 240 km and 90° , respectively, in their model. The range of rheology functions and slab parameters explored by *Conrad and Hager* [1999] is therefore too limited to support the general applicability of the isoviscous scaling (equation (1)). The concept of effective viscosity is useful as it quantifies the relation between the average strain rate and the average stress, but the scaling of bending dissipation, e.g., how dissipation varies with the bending curvature, requires more than this zeroth-order parameterization.

[43] Inferring mantle dynamics from observational constraints tends to suffer from nonuniqueness. The radius of curvature, for example, is inversely correlated with dip angle in the real subduction zones (i.e., more steeply dipping slabs tend to have smaller radii), and a similar behavior observed in free subduction models may seem to support those models [e.g., *Capitanio et al.*, 2009]. Such inverse relation, instead, may simply imply that real plates lose their strength at greater depths so bending happens only at relatively shallow depths. The combination of a large curvature (e.g., 600 km) and a large dip (e.g., 90°) means bending deformation over a considerable depth range (e.g., 0–600 km), and expecting a subducted plate to maintain its full strength down to the transition zone is probably unrealistic. Subducted slabs are gradually warmed up by the surrounding mantle, so because of temperature-dependent viscosity, this warming results in the gradual loss of plate strength. It is noted that heat transfer is usually neglected in free subduction models. Alternatively, the inverse correlation between radius and dip angle may be explained by the radius exponent varying from negative to positive as dip angle increases, as shown for some cases with pseudoplastic olivine rheology (Figures 9e and 9f).

[44] *Korenaga* [2010] conducted a total of 280 cases of self-consistent simulation of plate tectonic convection using pseudoplastic rheology, with a range of rheological parameters ($\sim 10 < \theta < \sim 30$ and $0.1 \leq \gamma \leq 1$, corresponding to $\Delta\eta_L$ of up to $\sim 10^4$) and the internal Rayleigh number (from $\sim 10^5$ to 10^{10}). The ratio of viscous dissipation within the top thermal boundary (mostly due to bending) over the total dissipation varies considerably among different cases, ranging from ~ 0.1 to ~ 0.9 . Bending dissipation can be either significant or trivial, and the self-consistent generation of plate tectonics by itself does not seem to demand either way. Previous suggestions based on modeling with a limited exploration of rheological function may thus be viewed with caution. To understand a likely role of bending dissipation in plate tectonics, it is imperative to better understand the physics of lithospheric damage [e.g., *Korenaga*, 2007] as well as to explore extensively the plausible parameter space of mantle rheology [*Korenaga and Karato*, 2008]. The nonuniqueness of geodynamical inference is enhanced quite considerably by the uncertainty of mantle rheology, but unfortunately, this issue tends to be underestimated in the studies of global mantle flow, in which a primary focus is to

Table A1. Slab Parameters and Energy Balance for Global Subduction Zones

ID	ϕ ($^{\circ}$)	R (km)	v (mm/yr)	t (Ma)	W (km)	L (km)	Φ_{PE} (GW)	$\Phi_{PE,2}/\Phi_{PE}$	Φ_{BE}^{strong} (GW)	Φ_{BE}^{weak} (GW)
ANDA6	70	340	2.0	85.5	236.7	600	0.80	0.26	0.97	0.09
ANDA5	70	350	11.8	82.0	225.8	600	4.45	0.27	5.71	0.63
ANDA4	70	360	8.1	77.8	225.8	600	3.01	0.27	3.70	0.36
ANDA3	70	380	14.2	73.7	230.2	670	5.77	0.26	6.68	0.69
ANDA2	70	400	22.9	69.2	205.7	670	8.18	0.28	9.04	0.86
ANDA1	56	530	20.4	61.1	226.6	670	6.72	0.28	5.59	0.60
SUM6	40	530	38.6	51.8	366.8	1200	21.74	0.13	7.42	1.52
SUM5	40	540	25.2	46.2	314.5	1200	11.53	0.13	4.09	0.77
SUM4	49	540	31.8	47.1	265.2	1200	15.03	0.16	6.41	0.81
SUM3	49	550	33.7	60.0	290.3	1200	19.72	0.16	9.37	1.24
SUM2	61	580	34.9	69.0	239.4	1200	22.17	0.21	12.74	1.14
SUM1	63	600	46.3	72.0	348.9	1200	45.34	0.22	26.66	2.36
JAVA7	71	540	49.2	75.0	228.2	1200	34.42	0.23	23.87	1.78
JAVA6	68	540	55.1	78.0	219.0	1200	36.52	0.22	26.10	2.10
JAVA5	68	540	59.0	80.0	198.3	1200	35.85	0.22	27.41	5.38
JAVA4	69	530	60.9	81.0	222.1	1200	41.98	0.22	32.77	6.60
JAVA3	68	520	62.0	82.0	219.3	1200	41.81	0.21	31.36	4.69
JAVA2	68	500	63.8	83.0	199.7	1200	39.06	0.21	30.93	4.57
JAVA1	70	480	65.8	84.0	196.6	1200	40.37	0.20	34.64	3.74
TIM1	56	460	39.1	141.0	219.3	670	17.99	0.24	22.37	2.46
TIM2	56	600	31.3	141.0	220.9	670	15.72	0.30	17.37	1.44
TIM3	56	500	25.3	141.0	232.2	670	12.62	0.26	15.13	1.49
TIM4	56	360	25.1	141.0	232.9	670	11.53	0.20	15.65	2.20
TIM5	56	260	25.4	141.0	222.7	670	10.45	0.14	4.31	3.53
TAN1	56	260	9.6	54.0	222.9	500	1.95	0.20	0.64	0.40
TAN2	56	400	6.3	54.0	223.2	500	1.43	0.28	1.45	0.17
TAN3	56	500	0.4	54.0	343.3	500	0.15	0.33	0.05	0.01
TAN4	56	386	14.2	54.0	222.3	500	3.18	0.27	3.33	0.43
SER1	56	318	49.8	54.0	314.0	500	14.93	0.23	18.78	3.55
SER2	56	318	11.2	54.0	225.5	500	2.41	0.23	2.60	0.45
SER3	56	318	3.0	54.0	222.2	500	0.64	0.23	0.64	0.10
TOL0e	56	318	103.9	10.0	225.8	559	10.65	0.22	18.92	2.56
HALM2	56	318	18.6	40.0	225.8	400	2.93	0.28	3.33	0.56
HALM1	56	318	0.8	40.0	314.5	400	0.18	0.28	0.09	0.02
SANG3e	56	318	75.6	40.0	290.3	670	22.79	0.19	22.93	5.73
SANG2e	56	318	59.8	40.0	230.2	670	14.30	0.19	12.34	2.51
SANG1e	56	318	58.7	40.0	223.2	670	13.61	0.19	11.35	2.46
SULA2e	56	200	35.0	40.0	230.2	150	2.45	0.38	3.11	2.25
SULA1e	56	200	25.7	40.0	225.8	150	1.77	0.38	1.85	1.25
SULU2e	56	318	32.5	20.0	314.5	100	2.36	0.61	4.18	0.86
SULU1e	56	318	27.2	20.0	346.0	300	3.85	0.35	3.94	0.77
COTOe	56	318	32.2	40.0	223.2	559	6.46	0.22	5.71	1.01
NEG4e	55	318	16.6	20.0	290.3	300	1.93	0.34	1.91	0.37
NEG3e	55	318	22.2	20.0	290.3	300	2.58	0.34	2.75	0.56
NEG2e	55	318	16.8	20.0	225.8	300	1.52	0.34	1.56	0.33
NEG1e	55	318	8.0	20.0	314.5	300	1.01	0.34	1.03	0.16
LUZ4e	75	190	44.8	22.0	290.3	400	7.50	0.25	12.59	3.09
LUZ3	60	200	74.3	18.0	230.2	670	11.70	0.14	4.15	2.81
LUZ2	60	310	89.9	27.0	222.4	670	18.07	0.20	16.06	3.83
LUZ1	65	280	95.6	32.0	271.5	670	26.62	0.20	27.13	6.97
BAT2	75	220	71.8	35.0	256.8	670	20.73	0.18	26.96	6.60
BAT1	75	220	93.1	35.0	256.8	670	26.89	0.18	36.31	8.86
TAIW	56	318	91.6	54.0	256.8	670	28.31	0.18	33.03	8.29
PHIL7	56	160	15.5	50.0	245.4	250	1.71	0.22	1.33	1.09
PHIL6	56	170	18.3	50.0	217.9	250	1.82	0.23	1.43	1.09
PHIL5	56	180	29.5	50.0	223.2	250	3.05	0.24	2.93	2.36
PHIL4	56	180	30.3	50.0	206.7	250	2.91	0.24	2.52	2.26
PHIL3	56	200	45.7	50.0	216.2	250	4.73	0.26	5.79	4.61
PHIL2	56	240	58.8	45.0	236.7	150	4.87	0.43	6.33	4.95
PHIL1	56	240	43.7	40.0	236.7	100	2.78	0.53	2.45	2.44
RYUS	65	340	94.2	35.0	204.2	450	16.11	0.31	21.88	8.06
RYUN1	57	380	86.0	38.0	247.6	450	16.97	0.30	22.70	4.60
RYUN2	58	400	87.3	48.0	231.4	350	15.83	0.37	26.64	9.61
RYUN3	61	360	81.0	50.0	257.6	325	16.09	0.37	29.50	6.69
RYUN4	64	300	78.8	50.0	251.9	300	14.19	0.36	30.96	7.60
NAN3	56	800	46.9	17.0	208.5	100	4.14	0.81	5.90	4.71
NAN2	56	750	41.8	17.0	199.3	100	3.35	0.80	5.72	5.94
NAN1	56	750	37.1	21.0	189.2	100	3.13	0.80	4.42	0.29
SUR	56	318	17.7	54.0	192.6	100	1.26	0.60	3.70	0.59
PAL	56	318	0.9	54.0	312.3	350	0.21	0.30	0.13	0.04
YAP3	56	318	2.5	35.0	220.6	100	0.17	0.61	0.36	0.05
YAP2	56	318	3.3	30.0	342.1	100	0.32	0.61	0.64	0.10
YAP1	56	318	2.9	35.0	256.8	100	0.22	0.61	0.47	0.07
SMAR5	74	180	8.2	155.0	219.2	350	2.30	0.21	8.18	1.49

Table A1. (continued)

ID	ϕ (°)	R (km)	v (mm/yr)	t (Ma)	W (km)	L (km)	Φ_{PE} (GW)	$\Phi_{PE,2}/\Phi_{PE}$	Φ_{BE}^{strong} (GW)	Φ_{BE}^{weak} (GW)
SMAR4	64	200	15.0	155.0	200.3	400	3.97	0.19	3.19	2.51
SMAR3	73	220	55.1	156.0	212.9	500	20.96	0.20	69.83	18.31
SMAR2	74	270	66.0	156.3	291.0	900	58.92	0.15	111.76	25.93
SMAR1	84	280	69.7	153.2	211.8	900	48.18	0.18	100.98	19.98
NMAR4	86	280	62.5	149.6	222.4	900	45.29	0.19	95.19	18.08
NMAR3	86	280	41.2	147.5	236.7	900	31.56	0.19	61.49	10.33
NMAR2	84	300	27.2	146.6	314.5	900	27.78	0.20	46.04	4.52
NMAR1	72	280	17.8	145.3	253.3	900	13.23	0.16	18.73	2.03
IZU5	64	260	43.4	150.0	225.8	670	20.71	0.16	46.12	11.49
IZU4	74	320	49.0	148.0	222.4	670	26.68	0.23	53.93	8.95
IZU3	71	340	44.9	141.0	210.4	670	22.31	0.23	39.05	4.65
IZU2	61	360	51.2	135.0	205.3	670	21.87	0.21	33.53	4.97
IZU1	50	400	55.0	129.0	202.3	670	19.39	0.20	24.44	4.31
JAP4	31	500	92.5	127.0	217.9	670	22.35	0.16	11.47	8.03
JAP3	31	560	91.6	132.0	226.8	670	23.97	0.17	10.10	8.01
JAP2	29	580	85.9	131.0	200.3	670	18.51	0.17	5.57	3.95
JAP1	25	580	90.2	128.0	216.5	670	17.67	0.15	5.45	3.99
SKOUR5	32	500	76.7	128.0	207.3	670	18.31	0.16	6.16	4.19
SKOUR4	33	420	73.5	120.0	191.2	670	15.72	0.14	8.81	6.46
SKOUR3	40	410	77.0	118.0	191.1	670	19.80	0.16	8.93	7.28
SKOUR2	44	380	70.8	118.0	163.9	670	16.92	0.17	21.31	6.55
SKOUR1	47	360	77.5	118.0	195.2	670	23.27	0.17	33.50	10.56
NKOUR3	48	360	79.4	110.0	251.2	900	38.84	0.13	40.86	13.21
NKOUR2	50	360	78.0	110.0	282.5	850	42.39	0.15	52.34	14.83
NKOUR1	51	360	76.8	110.0	237.9	850	35.78	0.15	44.49	12.52
KAM2	56	360	74.9	100.0	222.4	670	27.81	0.20	42.08	9.82
KAM1	64	340	73.8	100.0	256.8	400	23.95	0.32	58.06	12.95
W_ALE1	56	210	21.9	45.0	137.8	300	1.60	0.24	0.70	0.61
W_ALE2	56	220	36.1	45.0	130.3	300	2.52	0.25	1.58	1.29
C_ALE1	56	240	25.4	54.0	137.7	350	2.36	0.24	0.93	0.78
C_ALE2	57	270	41.1	56.0	129.6	400	4.25	0.24	6.44	1.39
C_ALE3	57	270	52.0	58.0	144.3	475	6.95	0.21	10.12	2.42
C_ALE4	58	270	60.2	58.0	128.8	550	8.20	0.19	11.89	3.40
C_ALE5	59	280	61.4	58.0	129.4	550	8.59	0.20	12.91	3.41
C_ALE6	62	280	59.5	63.0	127.6	500	8.28	0.23	14.54	3.66
E_ALE1	61	290	65.3	63.0	130.6	500	9.25	0.23	15.89	3.89
E_ALE2	60	310	65.7	61.0	133.0	450	8.65	0.26	14.80	3.68
E_ALE3	59	310	64.9	59.0	132.3	450	8.24	0.26	13.88	3.44
E_ALE4	56	260	64.3	58.0	132.5	400	6.73	0.23	5.25	3.84
E_ALE5	53	300	63.1	53.0	128.4	400	6.04	0.25	10.11	2.78
W_ALA1	48	400	61.4	52.0	124.5	400	5.55	0.29	6.57	1.30
W_ALA2	47	400	60.5	52.0	124.0	400	5.33	0.29	6.37	1.17
W_ALA3	47	520	59.4	52.0	123.5	300	4.76	0.41	5.79	1.07
W_ALA4	47	550	58.0	52.0	138.9	300	5.36	0.43	6.55	0.99
W_ALA5	45	600	58.0	49.0	127.1	300	4.70	0.44	6.41	2.00
E_ALA1	43	660	56.6	46.0	123.7	300	4.27	0.45	5.37	1.27
E_ALA2	40	880	51.4	45.0	146.1	300	4.74	0.51	3.70	1.53
E_ALA3	38	930	48.0	40.0	150.6	300	4.13	0.51	3.04	1.19
E_ALA4	40	1120	42.9	39.0	159.0	200	3.93	0.67	5.01	1.53
E_ALA5	40	1200	52.0	39.0	117.9	200	3.71	0.68	4.61	1.27
CASC1	45	500	43.8	5.0	256.8	400	2.58	0.34	1.62	0.26
CASC2	45	840	36.2	10.0	245.4	300	3.07	0.53	2.90	0.42
CASC3	45	767	30.3	11.0	225.8	300	2.36	0.51	1.88	0.17
CASC4	45	767	24.3	11.0	223.2	300	1.87	0.51	1.52	0.16
CASC5	45	960	26.6	10.0	222.4	300	2.20	0.57	2.05	0.21
MEX1	56	280	39.7	8.0	328.2	300	3.25	0.32	0.79	0.54
MEX2	56	310	47.5	8.0	232.7	300	2.85	0.35	2.15	0.45
MEX3	56	440	51.5	15.0	212.8	300	4.44	0.43	4.40	0.74
MEX4	56	340	55.7	15.0	204.9	300	4.15	0.36	3.66	0.71
MEX5	56	400	59.5	15.0	202.1	300	4.67	0.40	4.37	0.70
MEX6	56	440	60.6	15.0	196.5	300	4.82	0.43	4.79	0.65
COST1	55	340	63.6	18.0	225.4	300	5.59	0.36	5.47	1.15
COST2	54	280	68.6	22.0	219.5	400	7.31	0.25	8.32	2.22
COST3	64	260	73.0	24.0	211.1	400	8.95	0.27	12.11	3.02
COST4	66	240	77.6	28.0	233.8	400	11.40	0.26	17.82	4.37
COST5	57	260	83.6	26.0	219.4	400	9.97	0.24	6.37	3.47
COST6	59	540	77.6	16.0	220.0	100	5.56	0.75	11.01	10.93
COL1	50	380	42.3	19.0	256.8	670	7.31	0.20	3.46	0.69
COL2	45	400	46.6	15.0	314.5	670	7.99	0.19	1.05	0.72
COL3	45	420	41.3	12.0	290.3	670	5.91	0.20	1.78	0.51
COL4	47	500	39.2	15.0	245.4	670	5.76	0.24	2.30	0.47
COL5	47	520	36.0	16.0	230.2	670	5.18	0.25	2.30	0.46
PER1	45	520	69.1	30.0	200.5	1200	18.12	0.15	7.40	1.64
PER2	46	520	70.9	30.0	200.0	1200	18.94	0.15	7.75	2.49

Table A1. (continued)

ID	ϕ (°)	R (km)	v (mm/yr)	t (Ma)	W (km)	L (km)	Φ_{PE} (GW)	$\Phi_{PE,2}/\Phi_{PE}$	Φ_{BE}^{strong} (GW)	Φ_{BE}^{weak} (GW)
PER3	47	520	70.7	31.0	208.2	1200	20.39	0.15	7.68	3.48
PER4	49	540	70.2	31.0	224.2	1200	22.80	0.16	10.92	6.14
PER5	49	490	69.3	46.0	233.3	1200	28.03	0.15	15.59	4.97
PER6	52	400	68.6	46.0	248.4	1200	30.21	0.13	15.40	2.72
PER7	49	340	66.6	46.0	222.4	1200	24.44	0.11	3.44	2.86
NCHI1	50	360	58.1	52.0	330.9	1200	34.53	0.11	17.68	3.60
NCHI2	41	520	63.5	54.0	240.0	1200	24.41	0.13	10.33	2.82
NCHI3	40	620	72.2	55.0	201.0	1100	21.84	0.16	9.85	2.92
NCHI4	45	700	71.3	54.0	201.2	1000	22.87	0.22	11.90	2.97
NCHI5	47	700	70.8	53.0	201.5	900	21.73	0.24	12.79	3.69
NCHI6	49	400	68.5	52.0	201.2	800	17.44	0.17	12.00	2.47
JUAN1	56	300	68.7	49.0	204.5	670	15.93	0.18	18.01	4.62
JUAN2	56	240	70.8	48.0	198.4	670	15.15	0.14	7.65	5.51
JUAN3	56	280	70.6	48.0	202.2	670	15.82	0.17	17.45	4.86
SCHI1	35	440	65.6	42.0	220.0	670	10.31	0.16	1.96	1.45
SCHI2	35	500	61.6	39.0	219.8	559	8.25	0.21	1.46	1.15
SCHI3	35	550	72.6	35.0	208.7	559	8.95	0.23	2.20	1.35
SCHI4	35	540	75.5	33.0	230.2	559	9.93	0.23	5.70	1.61
SCHI5	35	450	76.2	20.0	222.4	559	7.26	0.20	5.82	1.15
TRI1	56	410	76.0	12.0	222.4	559	8.97	0.27	8.44	2.66
TRI2	56	410	76.1	5.0	222.4	559	5.82	0.28	4.09	7.18
TRI3	56	410	20.8	10.0	223.2	559	2.25	0.27	1.44	0.30
TRI4	56	410	20.9	18.0	222.4	559	3.01	0.27	1.84	0.34
PAT1	56	318	19.3	18.0	236.7	559	2.77	0.22	1.73	0.35
PAT2	56	318	18.8	20.0	230.2	559	2.77	0.22	1.80	0.38
PAT3	56	318	12.0	20.0	314.5	559	2.41	0.22	1.59	0.33
BARB1	55	580	12.7	117.0	225.8	670	5.78	0.29	5.78	0.49
BARB2	55	460	11.9	110.0	223.2	670	4.86	0.24	5.15	0.54
ANTI1	56	450	10.8	98.0	230.2	670	4.35	0.24	4.43	0.48
ANTI2	56	420	9.6	90.0	314.5	670	4.97	0.23	5.06	0.53
ANTI3	56	400	5.9	84.0	223.4	500	1.66	0.28	2.02	0.22
PORTO1	56	300	8.1	92.0	210.0	500	2.07	0.22	2.77	0.47
PORTO2	56	230	7.2	100.0	210.0	500	1.80	0.17	0.61	0.56
PORTO3	56	180	7.2	110.0	209.4	500	1.80	0.12	0.72	0.76
FRAN	56	318	2.6	117.0	216.4	500	0.78	0.22	1.16	0.17
SAND1	72	240	35.7	33.0	271.5	670	10.51	0.19	11.20	1.75
SAND2	83	240	78.0	36.0	223.2	670	21.40	0.22	29.61	6.22
SAND3	84	220	72.4	40.0	290.3	670	26.79	0.21	41.68	9.20
SAND4	86	160	35.1	40.0	140.2	670	5.92	0.16	9.75	2.57
SAND5	80	160	15.1	40.0	128.3	670	2.26	0.14	2.66	0.48
SAND6	81	204	3.6	40.0	132.8	670	0.59	0.18	0.66	0.08
PUY	56	318	23.8	33.0	271.5	150	2.26	0.51	4.50	0.77
HIKS1	56	320	17.7	54.0	314.5	670	6.71	0.19	5.84	0.94
HIKS2	56	480	13.3	54.0	314.5	670	5.56	0.26	4.44	0.50
HIKS3	56	460	38.0	54.0	225.8	670	11.27	0.25	9.13	1.09
HIKN1	56	310	40.8	54.0	225.8	670	11.03	0.18	10.42	1.77
HIKN2	56	280	43.8	45.0	230.2	670	10.82	0.17	9.85	2.19
KER1	70	260	46.6	95.0	200.5	900	21.64	0.14	29.75	6.34
KER2	68	220	51.4	97.0	206.4	1000	26.06	0.11	36.49	10.21
KER3	62	260	54.3	99.0	213.9	1100	30.16	0.11	34.35	9.66
KER4	57	270	59.6	101.0	212.0	1200	33.85	0.09	32.25	10.10
KER5	56	280	64.1	103.0	201.9	1300	37.29	0.09	34.42	10.25
TONG1	57	280	71.2	105.0	202.4	670	23.74	0.16	40.01	11.59
TONG2	54	300	103.9	106.0	227.2	670	37.79	0.16	61.03	18.13
TONG3	51	300	153.0	107.0	215.8	670	50.48	0.15	34.54	25.20
TONG4	53	300	182.1	108.0	208.3	670	60.29	0.16	97.68	30.14
TONG5	55	320	205.4	108.0	204.4	670	69.82	0.18	119.62	33.29
TONG6	55	305	223.2	109.0	221.9	670	81.94	0.17	136.96	40.86
SHEB1	66	160	71.4	46.0	291.5	500	18.12	0.14	15.54	11.81
SHEB2	71	160	118.6	45.0	224.2	670	30.93	0.12	20.24	15.79
SHEB3	68	160	99.3	48.0	200.4	670	23.27	0.12	15.10	12.19
ENR	56	180	38.3	56.0	256.8	670	10.97	0.10	7.34	5.50
NHEB1	82	140	107.6	60.0	230.2	670	34.80	0.12	26.35	23.29
NHEB2	72	120	165.5	60.0	283.8	670	60.91	0.09	61.73	44.07
SALOM4	56	318	141.0	31.0	240.9	500	24.72	0.24	29.29	9.00
SALOM3	56	318	27.0	31.0	241.0	670	5.96	0.19	4.15	0.79
SALOM2	56	318	55.1	31.0	241.3	670	12.18	0.19	8.39	1.88
SALOM1	56	318	65.7	31.0	242.2	500	11.58	0.24	11.14	2.57
BOUG2	56	130	102.3	31.0	254.4	500	16.05	0.10	15.86	9.83
BOUG1	56	140	93.8	31.0	255.2	670	19.42	0.08	13.34	8.71
BRET3	79	180	120.0	31.0	235.3	670	29.60	0.16	41.05	10.99
BRET2	82	260	75.2	31.0	243.6	670	21.23	0.23	26.78	5.50
BRET1	76	220	64.0	31.0	202.6	670	13.85	0.19	17.07	4.13

find a model that can satisfy given observables and its uniqueness is rarely discussed.

5. Summary

[45] By designing a fan-shaped fluid dynamical model with appropriate kinematic boundary conditions, we were able to capture the essence of the bending deformation field associated with subduction. The computational efficiency of instantaneous Stokes flow calculations allowed us to explore exhaustively the four-dimensional slab parameter space (dip, age, radius of curvature, and velocity), and we estimated the scaling of bending dissipation for a range of viscosity functions, including one isoviscous case, 10 purely temperature-dependent viscosity cases, 60 pseudoplastic rheology cases, and 30 pseudoplastic olivine rheology cases.

[46] Our scaling for the isoviscous case is similar to what is commonly assumed for bending dissipation, but even in this simplest case, the age and radius exponents exhibit dip dependency. As we move away from the isoviscous case toward more mantle-like rheology, we observe that the conventional scaling falls down gradually owing to the increasing complexity of the bending deformation field. Because there has been no consensus on weakening mechanisms that compensate the strongly temperature-dependent rheology of mantle minerals, it is still unclear which of our scaling laws would be most relevant to the subduction zones on Earth. It is probably safe to conclude, however, that approximating plate rheology with constant ‘effective’ viscosity, which has been common in studies on subduction dynamics, likely limits the potential relevance of these studies to the real Earth. It is still premature to conclude whether or not bending dissipation would be significant on a global scale, because it depends largely on assumed mantle rheology, and for a better understanding of the physics of plate tectonics, further theoretical studies that properly honor the complexity of mantle rheology appear to be essential.

Appendix A: Numerical Results on Global Subduction Zones

[47] Table A1 shows slab parameters for all of subduction zones, based on the compilations of *Lallemant et al.* [2005] and *Wu et al.* [2008] with some adjustments as described in section 4.2. Listed slab parameters are dip angle ϕ , the radius of curvature R , plate velocity v , plate age t , the width of a subduction zone W , and the length of a subducted plate L . The rate of gravitational potential energy release Φ_{PE} is calculated from these parameters, and the column $\Phi_{PE,2}/\Phi_{PE}$ lists the ratio of the contribution from the bending part. The rate of bending dissipation is calculated using pseudoplastic rheology with KK08 flow laws and $T_{\max} = 700^\circ\text{C}$, and $\Phi_{BE}^{\text{strong}}$ is for the case with $\mu = 0.8$, and Φ_{BE}^{weak} for $\mu = 0.1$.

[48] **Acknowledgments.** This work was sponsored by the U.S. National Science Foundation under grant EAR-0449517 and Microsoft A. Richard Newton Breakthrough Research Award. The manuscript has benefited from comments and suggestions by Associate Editor Ctirad Matyska, Jeroen van Hunen, and an anonymous reviewer.

References

- Ave Lallemant, H. G., J.-C. C. Mercier, N. L. Carter, and J. V. Ross (1980), Rheology of the upper mantle: Inferences from peridotite xenoliths, *Tectonophysics*, *70*, 85–113.
- Becker, T. W., C. Faccenna, R. J. O’Connell, and D. Giardini (1999), The development of slabs in the upper mantle: Insights from numerical and laboratory experiments, *J. Geophys. Res.*, *104*, 15,207–15,226.
- Bellahsen, N., C. Faccenna, and F. Funiciello (2005), Dynamics of subduction and plate motion in laboratory experiments: Insights into the “plate tectonics” behavior of the Earth, *J. Geophys. Res.*, *110*, B01401, doi:10.1029/2004JB002999.
- Bercovici, D. (2003), The generation of plate tectonics from mantle convection, *Earth Planet. Sci. Lett.*, *205*, 107–121.
- Bercovici, D., Y. Ricard, and M. A. Richards (2000), The relation between mantle dynamics and plate tectonics: A primer, in *The History and Dynamics of Global Plate Motions*, *Geophys. Monogr. Ser.*, vol. 121, edited by M. A. Richards, R. G. Gordon, and R. D. van der Hilst, pp. 5–46, AGU, Washington, D. C.
- Buffett, B. A. (2006), Plate force due to bending at subduction zones, *J. Geophys. Res.*, *111*, B09405, doi:10.1029/2006JB004295.
- Byerlee, J. (1978), Friction of rocks, *Pure Appl. Geophys.*, *116*, 615–626.
- Capitani, F. A., G. Morra, and S. Goes (2007), Dynamic models of downgoing plate-buoyancy driven subduction: Subduction motions and energy dissipation, *Earth Planet. Sci. Lett.*, *262*, 284–297.
- Capitani, F. A., G. Morra, and S. Goes (2009), Dynamics of plate bending at the trench and slab-plate coupling, *Geochem. Geophys. Geosyst.*, *10*, Q04002, doi:10.1029/2008GC002348.
- Condie, K. C., and V. Pease (Eds.) (2008), *When Did Plate Tectonics Begin on Planet Earth?*, Geol. Soc. of Am., Boulder, Colo.
- Conrad, C. P., and B. H. Hager (1999), Effects of plate bending and fault strength at subduction zones on plate dynamics, *J. Geophys. Res.*, *104*, 17,551–17,571.
- Di Giuseppe, E., J. van Hunen, F. Funiciello, C. Faccenna, and D. Giardini (2008), Slab stiffness control of trench motion: Insights from numerical models, *Geochem. Geophys. Geosyst.*, *9*, Q02014, doi:10.1029/2007GC001776.
- Evans, R. L., G. Hirth, K. Baba, D. Forsyth, A. Chave, and R. Mackie (2005), Geophysical evidence from the MELT area for compositional controls on oceanic plates, *Nature*, *437*, 249–252.
- Goetze, C., and B. Evans (1979), Stress and temperature in the bending lithosphere as constrained by experimental rock mechanics, *Geophys. J. R. Astron. Soc.*, *59*, 463–478.
- Gurnis, M., S. Zhong, and J. Toth (2000), On the competing roles of fault reactivation and brittle failure in generating plate tectonics from mantle convection, in *The History and Dynamics of Global Plate Motions*, *Geophys. Monogr. Ser.*, vol. 121, edited by M. A. Richards, R. G. Gordon, and R. D. van der Hilst, pp. 73–94, AGU, Washington, D. C.
- Hirth, G., and D. L. Kohlstedt (1996), Water in the oceanic mantle: Implications for rheology, melt extraction, and the evolution of the lithosphere, *Earth Planet. Sci. Lett.*, *144*, 93–108.
- Hirth, G., and D. Kohlstedt (2003), Rheology of the upper mantle and the mantle wedge: A view from the experimentalists, in *Inside the Subduction Factory*, *Geophys. Monogr. Ser.*, vol. 138, edited by J. Eiler, pp. 83–105, AGU, Washington, D. C.
- Karato, S., and P. Wu (1993), Rheology of the upper mantle: A synthesis, *Science*, *260*, 771–778.
- Kohlstedt, D. L., B. Evans, and S. J. Mackwell (1995), Strength of the lithosphere: Constraints imposed by laboratory experiments, *J. Geophys. Res.*, *100*, 17,658–17,602.
- Korenaga, J. (2006), Archean geodynamics and the thermal evolution of Earth, in *Archean Geodynamics and Environments*, *Geophys. Monogr. Ser.*, vol. 164, edited by K. Benn, J.-C. Mareschal, and K. Condie, pp. 7–32, AGU, Washington, D. C.
- Korenaga, J. (2007), Thermal cracking and the deep hydration of oceanic lithosphere: A key to the generation of plate tectonics?, *J. Geophys. Res.*, *112*, B05408, doi:10.1029/2006JB004502.
- Korenaga, J. (2010), Scaling of plate-tectonic convection with pseudoplastic rheology, *J. Geophys. Res.*, *115*, B11405, doi:10.1029/2010JB007670.
- Korenaga, J., and T. H. Jordan (2003), Physics of multiscale convection in Earth’s mantle: Onset of sublithospheric convection, *J. Geophys. Res.*, *108*(B7), 2333, doi:10.1029/2002JB001760.
- Korenaga, J., and S. Karato (2008), A new analysis of experimental data on olivine rheology, *J. Geophys. Res.*, *113*, B02403, doi:10.1029/2007JB005100.
- Krien, Y., and L. Fleitout (2008), Gravity above subduction zones and forces controlling plate motions, *J. Geophys. Res.*, *113*, B09407, doi:10.1029/2007JB005270.
- Lallemant, S., A. Heuret, and D. Boutelier (2005), On the relationships between slab dip, back-arc stress, upper plate absolute motion, and

- crustal nature in subduction zones, *Geochem. Geophys. Geosyst.*, 6, Q09006, doi:10.1029/2005GC000917.
- Landuyt, W., D. Bercovici, and Y. Ricard (2008), Plate generation and two-phase damage theory in a model of mantle convection, *Geophys. J. Int.*, 174, 1065–1080.
- Leng, W., and S. Zhong (2010), Constraints on viscous dissipation of plate bending from compressible mantle convection, *Earth Planet. Sci. Lett.*, 297, 154–164.
- Moresi, L., and V. Solomatov (1998), Mantle convection with a brittle lithosphere: Thoughts on the global tectonic styles of the Earth and Venus, *Geophys. J. Int.*, 133, 669–682.
- Parmentier, E. M., D. L. Turcotte, and K. E. Torrance (1976), Studies of finite amplitude non-Newtonian thermal convection with application to convection in the Earth's mantle, *J. Geophys. Res.*, 81, 1839–1846.
- Schellart, W. P. (2009), Evolution of the slab bending radius and the bending dissipation in the three-dimensional subduction models with a variable slab to upper mantle viscosity ratio, *Earth Planet. Sci. Lett.*, 288, 309–319.
- Schubert, G., D. L. Turcotte, and P. Olson (2001), *Mantle Convection in the Earth and Planets*, Cambridge Univ. Press, New York.
- Solomatov, V. S. (1995), Scaling of temperature- and stress-dependent viscosity convection, *Phys. Fluids*, 7, 266–274.
- Solomatov, V. S. (2004), Initiation of subduction by small-scale convection, *J. Geophys. Res.*, 109, B01412, doi:10.1029/2003JB002628.
- Solomatov, V. S., and L.-N. Moresi (2000), Scaling of time-dependent stagnant lid convection: Application to small-scale convection on earth and other terrestrial planets, *J. Geophys. Res.*, 105, 21,795–21,817.
- Stegman, D. R., J. Freeman, W. P. Schellart, L. Moresi, and D. May (2006), Influence of trench width on subduction hinge retreat rates in 3-D models of slab rollback, *Geochem. Geophys. Geosyst.*, 7, Q03012, doi:10.1029/2005GC001056.
- Tackley, P. J. (2000), Self-consistent generation of tectonic plates in time-dependent, three-dimensional mantle convection simulations: 2. Strain weakening and asthenosphere, *Geochem. Geophys. Geosyst.*, 1(8), 1026, doi:10.1029/2000GC000043.
- Turcotte, D. L., and G. Schubert (1982), *Geodynamics: Applications of Continuum Physics to Geological Problems*, John Wiley, New York.
- Wu, B., C. P. Conrad, A. Heuret, C. Lithgow-Bertelloni, and S. Lallemand (2008), Reconciling strong slab pull and weak plate bending: The plate motion constraint on the strength of mantle slabs, *Earth Planet. Sci. Lett.*, 272, 412–421.
- Zhong, S., and M. Gurnis (1993), Dynamic feedback between a continent-like raft and thermal convection, *J. Geophys. Res.*, 98, 12,219–12,232.

J. Korenaga, Department of Geology and Geophysics, PO Box 208109, Yale University, New Haven, CT 06520-8109, USA. (jun.korenaga@yale.edu)

I. R. Rose, Department of Earth and Planetary Science, University of California, Berkeley, CA 94720-4767, USA. (ian.rose@berkeley.edu)